

Copyright  
by  
Arash Shushtarian  
2016

**The Thesis Committee for Arash Shushtarian  
Certifies that this is the approved version of the following thesis:**

**Effect of a Discrete Three-Phase Methane Equilibrium Zone on the  
Bottom-Simulating Reflection**

**APPROVED BY  
SUPERVISING COMMITTEE:**

**Supervisor:**

---

Hugh Daigle

---

Kamy Sepehrnoori

**Effect of a Discrete Three-Phase Methane Equilibrium Zone on the  
Bottom-Simulating Reflection**

**by**

**Arash Shushtarian, B.S.**

**Thesis**

Presented to the Faculty of the Graduate School of

The University of Texas at Austin

in Partial Fulfillment

of the Requirements

for the Degree of

**Master of Science in Engineering**

**The University of Texas at Austin**

**December 2016**

## **Dedication**

I dedicate my thesis to my devoted loving parents,

Hamid and Sahar,

who lovingly supported me throughout my life.

I would also like to dedicate this work to my brother and sister,

Amir and Yasamin

To my grandmother, Soad, for her prayers,

To the rest of my family,

To friends.

## **Acknowledgements**

First and foremost, I would like to express my sincere appreciation to my graduate supervisor, Dr. Hugh Daigle for his constant encouragement, support, knowledge and unwavering patience throughout this project. My utmost gratitude to Dr. Kamy Sepehrnoori for committing himself not only to reading my thesis and providing valuable feedback, but also for all of his advice, guidance and insights during my academic studies

I am grateful to the U.S. Department of Energy as this project was partially supported by the Department of Energy under Award Number DE-FE0013919. I would also like to express my gratitude to the S.P. Yates Endowment for Graduate Fellowship in Petroleum Engineering and to Thurber's Memorial Endowed Presidential Scholarship in Engineering.

I wish to acknowledge Dr. Kyle Spikes and his PhD students, David Tang and Han Liu for introducing me to the subject of this study: synthetic seismogram. In addition, other members of the methane hydrate group; Abhishek Bihani, Ryan Andris, and Michael Nole provided insightful discussions and meetings; Mohammad Albusairi's introduction to IP was most useful/valuable

My deep gratitude to Frankie Hart, Amy Stewart, Leilani Swafford, and Mary Pettengill for their administrative and directorial help before and during my studies at the University of Texas at Austin.

Finally, I would like to thank Azor, Arjang, Cesar, and Nick for motivating and energizing me during these studies, and making these the best years of my life. I value the friendship of my friends in Iran and U.S, especially Sina Meymand, and many others for

believing in me and encouraging me to work harder and become a better person not only for myself but also for society.

## **Abstract**

# **Effect of a Discrete Three-Phase Methane Equilibrium Zone on the Bottom-Simulating Reflection**

Arash Shushtarian, M.S.E.

The University of Texas at Austin, 2016

Supervisor: Hugh Daigle

Marine gas hydrates are stable under conditions of low temperature and high pressure in the upper few hundreds of meters below the seafloor in a variety of geological setting. At a discrete horizon where thermodynamically favored phase switches from hydrate to gas, a characteristic seismic reflection referred as the bottom-simulating reflection (BSR) is produced. Furthermore, in sediments with a distribution of pore sizes, the gas and hydrate phases can coexist in pores of different sizes, giving a rise to three-phase equilibrium zone. This three-phase zone causes the BSR to have distinct characteristics that differ from those observed with a discrete phase boundary.

The main objective of this thesis is to model the seismic response of a potential three-phase zone at the Walker Ridge Block 313H in the northern Gulf of Mexico. I modeled the BSR arising from this three-phase zone and analyzed the characteristics of the BSR and their relationships to the thickness and phase saturation within the three-phase zone.

This was done by determining the elastic properties of the formation via rock physics models and their mathematical convolution with a seismic wavelet to create synthetic seismograms. Results show that the main factor for the intensity of the BSR is the abundance of the free gas in the three-phase zone. Free gas saturation as low as 5% in the three-phase zone is enough to make the BSR visible in synthetic seismograms regardless of the hydrate saturation.

Results of this thesis are significant for resource prospecting based on seismic data, drilling hazard identification, as well as the importance of hydrate as a potential source of energy and its influence on the global climate. For seismic prospecting, the presence of a three-phase zone inferred from BSR characteristic indicates the minimum methane flux into the base of the hydrate stability zone, and can be used to infer whether sufficient methane is available to form hydrate. For drilling hazard identification, the BSR characteristic indicates a possible shallower occurrence of gas than would be estimated under the assumption of a discrete phase boundary.

## Table of Contents

List of Tables .....	xii
List of Figures .....	xiii
Chapter 1: Introduction .....	1
1.1: Motivation and Research Objectives .....	1
1.2: Thesis Outline .....	2
Chapter 2: Literature Review .....	3
2.1: Gas Hydrate .....	3
2.1.1: Hydrate Occurrence .....	3
2.1.2: Methane Hydrate Stability and Occurrences .....	5
2.1.3: Structures of Gas Hydrate .....	7
2.1.4: Bottom-Simulating Reflection .....	9
2.2: Field Locations .....	11
2.2.1: Blake Ridge .....	11
2.2.2: Walker Ridge .....	12
2.3: Rock-Physics Models .....	15
2.3.1: Bulk Modulus of Pore Fluid .....	20
Sediments without Gas Hydrate .....	20
Sediments with Gas Hydrate .....	20
2.3.2: Dry Bulk and Shear Moduli .....	20
Hashin-Shtrikman Model .....	20
Wood Model .....	21
Hamilton Model .....	22
2.3.3: Sediments Mineralogy and Calculation .....	23
2.4: Synthetic Seismograms .....	23
Chapter 3: Methodology .....	27
3.1: Overview .....	27
3.2: Dry Modulus Models .....	27

3.3: Number of Contacts per Grain.....	30
3.4: Synthetic Seismogram .....	36
3.4.1: Overview.....	36
3.4.2: Wavelet Preparation.....	37
3.4.3: Interactive Petrophysics .....	38
Chapter 4: Data and Results.....	40
4.1: Overview.....	40
4.2: Velocity Profiles .....	40
4.2.1: Fluid Saturation.....	40
4.2.2: Fluid Saturation Comparison .....	45
4.2.3: 3-Phase Zone Thickness Variation .....	47
4.2.4: 3-Phase Zone Thickness Variation Comparison.....	51
4.3: Synthetic Seismogram .....	53
4.3.1: Fluid Saturation.....	53
Water-Hydrate-Free Gas Saturation (97-03-00-5m):.....	55
Water-Hydrate-Free Gas Saturation (92-03-05-5m):.....	55
Water-Hydrate-Free Gas Saturation (82-03-15-5m):.....	56
Water-Hydrate-Free Gas Saturation (67-03-30-5m):.....	56
Water-Hydrate-Free Gas Saturation (47-03-50-5m):.....	56
4.3.2: Thickness .....	57
Water-Hydrate-Free Gas Saturation (97-03-00-10m):.....	57
Water-Hydrate-Free Gas Saturation (92-03-05-10m):.....	58
Water-Hydrate-Free Gas Saturation (82-03-15-10m):.....	58
Water-Hydrate-Free Gas Saturation (67-03-30-10m):.....	58
Water-Hydrate-Free Gas Saturation (47-03-50-10m):.....	59
Water-Hydrate-Free Gas Saturation (92-03-05-30m):.....	59
Water-Hydrate-Free Gas Saturation (82-03-15-30m):.....	60
Water-Hydrate-Free Gas Saturation (47-03-50-30m):.....	60
4.4: Special Cases .....	60
4.4.1: Pure Hydrate .....	60

Water-Hydrate-Free Gas Saturation (90-10-00-5m):.....	63
Water-Hydrate-Free Gas Saturation (70-30-00-5m):.....	63
Water-Hydrate-Free Gas Saturation (50-50-00-5m):.....	64
4.4.2: High Hydrate with Low Free Gas .....	64
Water-Hydrate-Free Gas Saturation (49-50-01-5m):.....	67
Water-Hydrate-Free Gas Saturation (47-50-03-5m):.....	67
Water-Hydrate-Free Gas Saturation (45-50-05-5m):.....	67
4.5: Amplitude Versus Angle of Incidence .....	68
Fluid Saturation Comparison .....	68
Thickness .....	69
Pure Hydrate .....	69
High Hydrate with Low Free Gas .....	70
Chapter 5: Conclusion and Recommendations for Future Work .....	71
5.1: Summary and Conclusions .....	71
5.2: Recommendations for Future Work .....	72
Acronyms .....	73
Nomenclature .....	74
References .....	76

## List of Tables

Table 2.1:	Calculation parameters used in this study (Ecker et al., 2000). .....	23
Table 4.1:	Shows the values of amplitudes at an incidence angle of 0 and 45 degree for a 3-phase zone layer of 5 meters. A slight increase of amplitude occurs when hydrate saturation increases, while with an increase of gas the amplitude decreases. ....	68
Table 4.2:	Shows the values found for amplitudes at incidence angle of 0 and 45 degree, for a 3-phase zone layers containing constant hydrate saturation of 3%. Since the layers are heterogeneous at the reading points, only data from same thickness zone can be compared to one another. ....	69
Table 4.3:	Shows the values found for amplitudes at incidence angle of 0 and 45 degree, for layers containing high hydrate saturation. ....	69
Table 4.4:	Shows the values found for amplitudes at incidence angle of 0 and 45 degree, for layers containing high hydrate saturation and low gas saturation. ....	70

## List of Figures

- Figure 2.1: Worldwide map of recovered and inferred gas hydrates, from Council of Canadian Academies (2008). This map includes both permafrost and deepwater marine locations.....3
- Figure 2.2: Phase diagram for methane hydrate. This figure illustrates how pressure and temperature play a role on the stability of methane hydrates. Factors such as salinity and pore sizes also affect the stability of methane hydrate. Figure from NOAA Ocean Explorer 2010.....5
- Figure 2.3: An example of predominant signature of a bottom-simulating reflection from Blake Ridge in off-shore of South Carolina. Bottom-simulating reflections are not always as clearly visible. Figure from Paull and Matsumoto (2000).....7
- Figure 2.4: Three hydrate unit crystals and three natural structures of gas hydrates (Sloan, 1998).....8
- Figure 2.5: Illustration of a submarine sedimentary section containing gas hydrate (above) and free gas (below) the BSR (Haacke et al., 2007).....10
- Figure 2.6: Location map of Leg 164 sites on the southeastern North American continental margin. (Note: contours are in meters). Blake Ridge's Hole 995B is located in center part of Blake Ridge with coordinates: 31° 48.217' N, 75° 31.336' W with hole depth of 2776.9 meters/9110.6 feet below sea level (Paull et al.,1996). .....12

Figure 2.7: Northern Gulf of Mexico’s Bathymetric relief map (Frye et al., 2012). Walker Ridge’s 313H well is located at northwest part of Walker Ridge region with coordinates: 26° 39' 44.8482" N, 91° 40' 33.7467" W with water depth of 1966.3 meters/6451 feet below sea level and hole depth of 996.1 meters/3268 feet below sea floor (Collett et al.,2012).....13

Figure 2.8: Presents some of the raw (Gamma ray, resistivity, density, and  $V_p$ /compressional velocity), calibrated (Porosity), and calculated ( $V_p$  and  $V_s$ /shear velocity) data from WR 313H. All calculations are explained in the section 2.3.....14

Figure 2.9: Model A, the contact-cement model, assumes that hydrate cements the grain evenly. Model B, the no-contact-cement model for hydrate deposition among the grains (Ecker et al.,1998).....15

Figure 2.10: Graphical presentation of convolution process in creation of synthetic seismogram (Interactive Petrophysics, 2014). .....25

Figure 2.11: AVO’s 4 classification reference guide (Castagna et al., 1998). ....26

Figure 3.1: Reproduced figure from Guerin et al. (1999) for Blake Ridge ODP Leg 164 Hole 995B. Above ~440 mbsf and below ~520 mbsf the Wood and Hamilton model do not reflect or match the well-logging data. Equation (2.2) was used to find the bulk modulus for well-logging data. ....29

Figure 3.2: Orange line shows the compressional velocity for the model with an average of 4.5 contacts per grain. The model closely follows the same compressional velocity as the velocity from well-logging data from Walker Ridge 313H. ....31

Figure 3.3: Illustrates the compressional velocity model at Walker Ridge 313H for an average of 6.5 contacts per grain. By comparing this result with Figure 3.2, it can be observed that the compressional velocities have increased and the line has shifted.....32

Figure 3.4: Illustrates the compressional velocity model at Walker Ridge 313H for an average of 8.5 contacts per grain. In this case, compressional velocities are greater than those in Figure 3.2 and 3.3.....33

Figure 3.5: Illustrates the compressional velocity model at Walker Ridge 313H for an average of 8.5, 6.5, and 4.5 contacts per grain. As the number of contacts per grain decreases, calculated compressional velocity resembles more with the compressional velocity from well-logging data. ....35

Figure 3.6: Shows the wavelet used for seismic acquisition at Walker Ridge (S. Haines, personal communication).....37

Figure 3.7: Shows modified seismic wavelet used in Walker Ridge for Interactive Petrophysics requirements. ....38

Figure 4.1: This figure presents the compressional velocity versus depth where hydrate saturation is 1% in the 3-phase zone and gas saturation is increasing for each case (increasing gas saturation in 5 meters 3-phase zone) The compressional velocity does not change for the case where 1% hydrates are encountered. This is reasonable as hydrate do not change the elastic properties. As expected, when the gas saturation is increased, the compressional velocity decreases by 300 m/s for the first 5% gas substitution instead of water. As the gas content increases however, the increment of velocity drop, decreases to 250 m/s for 10% gas substitution. This decrease continues and reaches its minima 1200 m/s for 50% gas substitution. ....41

Figure 4.2: This figure presents the shear velocity versus depth for the same case as Figure 4.1, where 3-phase zone contains 1% hydrate saturation with increasing gas saturation. Results show that as the gas saturation increases, the shear velocity increases by a small amount. The shear velocity increases by about 10 m/s for each presented model as gas saturation increases. ....42

Figure 4.3: This figure presents the compressional velocity (on left) and shear velocity (on right) versus depth for a case where the hydrate saturation is 3% in 5 meters 3-phase zone with increasing free gas saturation. Results and conclusions are as same as the case with 1% hydrate saturation (Figures 4.1 and 4.2). ....43

Figure 4.4: This figure presents the compressional velocity (on left) and shear velocity (on right) versus depth for a case where the hydrate saturation is 5% in 5 meters 3-phase zone with increasing free gas saturation. ....44

- Figure 4.5: In high free gas saturation (on left) the hydrate saturation does not affect the compressional velocity. However, in low free gas saturation of 5%, small change of hydrate saturation is a factor in compressional velocity. ....45
- Figure 4.6: Comparison of shear velocity for sets two sets of models of 5% and 50% gas saturation with different hydrate saturation. The velocity difference between cases with 1%, 3%, and 5% hydrate saturation is so minimal that it is not observable. For each 2% increment increase of hydrate saturation, the shear velocity increases by 0.1 m/s. The same scenario applies to the sets of models with 50% gas saturation. ....46
- Figure 4.7: This figure presents the compressional velocity versus depth for a 3-phase zone with 3% hydrate saturation. The thickness is enough for the compressional velocity to reach its minimum. For example, for the case of “92-03-05”, the compressional velocity drops to 1600 m/s for 4 meters continuously. Furthermore, like the model presented in the previous section, as the gas saturation increases, the compressional velocity decreases. ....48
- Figure 4.8: This figure presents the shear velocity versus depth for the same cases as Figure 4.7, where 3-phase zone contains 3% hydrate saturation with increasing gas saturation. Like the results shown in the previous section, as the gas saturation increases, the shear velocity increases by a small amount. The shear velocity increases by about 10 m/s for each presented model for each increment increase of gas saturation. ....49

Figure 4.9: This figure presents the compressional velocity (on left) and shear velocity (on right) versus depth for a case where the hydrate saturation is 3% in a 30 m 3-phase zone with increasing free gas saturation. ....50

Figure 4.10: This figure presents the compressional velocity versus depth for all models containing 3% hydrate saturation with multiple free gas saturations and 3-phase zone thicknesses. ....52

Figure 4.11: Figure 4.11a shows the shear velocities for the same models in Figure 4.10. Since it is hard to follow and distinguish between each case, Figure 4.11b is presented. Figure 4.11b presents the same saturation models with different thickness zones of 5, 10, and 30 meters. ....53

Figure 4.12: Illustrates the seismic profile for Walker Ridge 313H where the porous media is saturated with water. Seismic reflections in this case are due to changes in porosity rather than fluid type. ....54

Figure 4.13: Synthetic seismograms for a 2-phase equilibrium zone containing 3% hydrate and zero free gas. The result looks similar to Figure 4.12 where layers are 100% saturated with water. Hydrates do not contribute in creation of BSR at low saturations. ....55

Figure 4.14: Seismic signature for a 3-phase equilibrium zone containing 3% hydrate and 5% free gas. As the free gas is substituted instead of water by 5% compared to the previous case (Figure 4.13), a profound seismic signature of BSR becomes observable around 880 mbsf. Compressional velocity greatly reduces as free gas is introduced in the model, which results in a strong negative reflection. ....55

Figure 4.15: Seismic signature for a 3-phase equilibrium zone containing 3% hydrate and 15% free gas. Compared to Figure 4.14, extra 10% free gas makes this seismic signature sharper and more profound.....56

Figure 4.16: Seismic signature for a 3-phase equilibrium zone containing 3% hydrate and 30% free gas. Due to the larger drop of compressional velocity, results show sharper peaks and troughs. As shown in compressional compression velocity curves, velocities for cases with high free gas saturation reach minima, which results in similar looking seismic signatures (BSRs).....56

Figure 4.17: Seismic signature for a 3-phase equilibrium zone containing 3% hydrate and 50% free gas.....56

Figure 4.18: Synthetic seismograms for a 10 m 3-phase equilibrium zone containing 3% hydrate and 0% free gas. Due to low hydrate saturation, no seismic reflections are seen. Results of this figure look identical to 5 m thickness model, Figure 4.13. ....57

Figure 4.19: Seismic signature for a 10 m 3-phase equilibrium zone containing 3% hydrate and 5% free gas. Comparing this model with the 5 m model, Figure 4.14, it is observable that the peak and trough of the seismic reflections are not squeezed against one another. ....58

Figure 4.20: Seismic signature for a 10 m 3-phase equilibrium zone containing 3% hydrate and 15% free gas. Compared to Figure 4.19, extra 10% free gas makes this seismic reflection sharper and more profound. ....58

Figure 4.21: Seismic signature for a 10 m 3-phase equilibrium zone containing 3% hydrate and 30% free gas. ....58

Figure 4.22: Seismic signature for a 10 m 3-phase equilibrium zone containing 3% hydrate and 50% free gas. ....	59
Figure 4.23: Seismic signature for a 3-phase equilibrium zone containing 3% hydrate and 5% free gas. Comparing this model with the 5 and 10 m models (Figure 4.14 and 4.19), the trough is not as strong in amplitude. In addition, the peaks of this seismic wavelet on both side of the trough are clear and distinguishable. ....	59
Figure 4.24: Seismic signature for a 3-phase equilibrium zone containing 3% hydrate and 15% free gas. Compared to Figure 4.23, the extra 10% free gas makes this seismic reflection stronger. ....	60
Figure 4.25: Seismic signature for a 3-phase equilibrium zone containing 3% hydrate and 50% free gas. The main trough of this model is what to be looked for when looking for the BSR. ....	60
Figure 4.26: This figure presents the compressional velocity versus depth for the cases with 10, 30 and 50% hydrate saturation and with a thickness of 5 m. As previously concluded, the compressional velocity does not increase with low hydrate saturations. The increase of hydrate saturation begins to be noticeable in layers with more than 10% hydrate saturation. Compressional velocity increases by ~20 m/s for each 10% increase of hydrate saturation. Unlike the case of free gas, where the compressional velocity reaches its minimum with the increase of free gas saturation, hydrate increases compressional velocity by ~20 m/s for each 10% hydrate increment until all pores are filled with hydrate. ....	61

- Figure 4.27: This figure presents the shear velocity versus depth for the Figure 4.26. The 5 m thick layer is filled with 10, 30, and 50% hydrate saturation. Results show that the hydrate saturation does not contribute or affect the shear velocity even in high hydrate saturation. ....62
- Figure 4.28: Seismic signature for a 2-phase zone containing 10% hydrate. Even though there is a slight increase of compressional velocity, the BSR is not visible. The result looks similar to Figure 4.12 where layers are 100% saturated with water. This shows that even 10% hydrate saturation does not contribute in the creation of the BSR. ....63
- Figure 4.29: Seismic signature for a 2-phase zone containing 30% hydrate. With this hydrate saturation, the BSR is now visible. As expected, since hydrate increases the compressional velocity, the BSR signature starts with a peak unlike free gas scenarios were trough. Observing peak simply implies that the layer encountered is denser than the layer above and compressional velocity is higher. ....63
- Figure 4.30. Seismic signature for a 2-phase zone containing 50% hydrate. The BSR is now visible and the peak is now easier to observe. Models in this section imply that hydrates are not the fluids to rely on when looking for the BSR, knowing that hydrates will not exceed 10% of the pores. .64

- Figure 4.31: This figure presents the compressional velocity versus depth for the cases with 50% hydrate saturation and increasing free gas of 1, 3, and 5% saturation. It appears that with 1% free gas saturation, the compressional velocity decreases by  $\sim 100$  m/s making its curve to almost match on top of 100% water saturation curve. For each extra 2% of free gas saturation, the compressional velocity continues to drop by  $\sim 120$  m/s. ....65
- Figure 4.32: This figure presents the shear velocity versus depth for the cases with 50% hydrate saturation and increasing free gas of 1, 3, and 5% saturation. As the water is substituted with hydrate and/or these low percentages of free gas, the shear velocity increases. However, these changes are minimal and hard to observe. ....66
- Figure 4.33: Seismic signature for a 3-phase zone containing 50% hydrate and 1% free gas (2-Phase zone containing 50% is presented in previous section, Figure 4.30). The BSR is now overshadowed due to presence of 1% free gas. This result matches with the compressional velocity result. Furthermore, this shows the importance of the free gas and how it can affect the BSR. ....67
- Figure 4.34: Seismic signature for a 3-phase zone containing 50% hydrate and 3% free gas. The addition of 2% free gas compared to the previous model will result in more reduction of the compressional velocity, thus making the BSR visible. ....67

Figure 4.35: Seismic signature for a 3-phase zone containing 50% hydrate and 5% free gas. As the free gas is substituted for water by 5% compared to the previous case, a profound seismic signature of BSR is created. This is due to a significant reduction in compressional velocity. ....67

Figure 4.36: Amplitude versus angle of incidence for model 92-03-05 with 3-phase zone thickness of 5 m. ....70

# Chapter 1: Introduction

## 1.1: MOTIVATION AND RESEARCH OBJECTIVES

The main objective of this thesis is to investigate the relationship between the seismic character of the bottom-simulating reflection at the base of the methane hydrate stability zone and the coexistence of water, hydrate, and methane gas in a discrete depth interval at the base of hydrate stability. This objective is motivated by the importance of hydrate as a potential source of energy, its influence on the global climate, drilling hazard identification, and seismic prospecting.

My approach to creating synthetic seismograms is to combine the study of rock physics with seismic convolution analysis to visually study the properties of the three-phase methane equilibrium zone on bottom-simulating reflectors. By varying the properties of the formation such as the thickness of the three-phase zone and the saturations within this zone and the layer below and above it, I was able to compare the reflection amplitude variation. These models are significant because they are important indicators of free gas at an interface and help to discriminate between different layers of fluid saturations.

Factors such as the formation velocity profiles, elastic properties, and synthetic seismograms confirm the explanation of the physical origin of the bottom-simulating reflectors. The key questions related to hydrate properties and the bottom-simulating reflector addressed in this study are the following:

- What are methane hydrates?
- What causes the bottom-simulating reflection?
- What are the elastic properties of hydrate-bearing sediments?
- Which rock physics models are best suited for this study?

- How to use acquired data from rock physic models and the actual wavelet to create synthetic seismograms?
- How to use these models to interpolate actual seismograms?

## **1.2: THESIS OUTLINE**

There are five chapters in this thesis. The following is a general overview of the material covered in each of the chapters:

Chapter 1 describes the importance of gas hydrates and the objective of this thesis.

Chapter 2 presents a description of the occurrence, stability, and three structures of gas hydrates and how these are related to bottom-simulating reflectors. Furthermore, rock-physics models are introduced and discussed.

Chapter 3 presents the procedures for the creation of synthetic seismograms. This includes a description of the wavelet, reflectance series, and the convolution process. In addition, there is a brief description of the steps in the process of using Interactive Petrophysics to create synthetic seismograms.

Chapter 4 presents the acoustic velocities and synthetic seismograms created based on different fluid saturation levels and three-phase zone thickness in a clay zone.

Chapter 5 gives a summary, conclusion and suggestions for future work.

## Chapter 2: Literature Review

### 2.1: GAS HYDRATE

#### 2.1.1: Hydrate Occurrence

Gas hydrate is an ice-like solid mixture composed of water and gas guest molecules. Gas hydrates are widely found in continental margin sediments, usually several hundreds of meters below the seafloor, as well as in onshore permafrost regions. Marine gas hydrates are stable within the sediment column in a depth interval of low temperature and high pressure (close to 0°C and elevated pressure conditions). In addition to favorable temperature and pressure, adequate amounts of water and methane are also required.

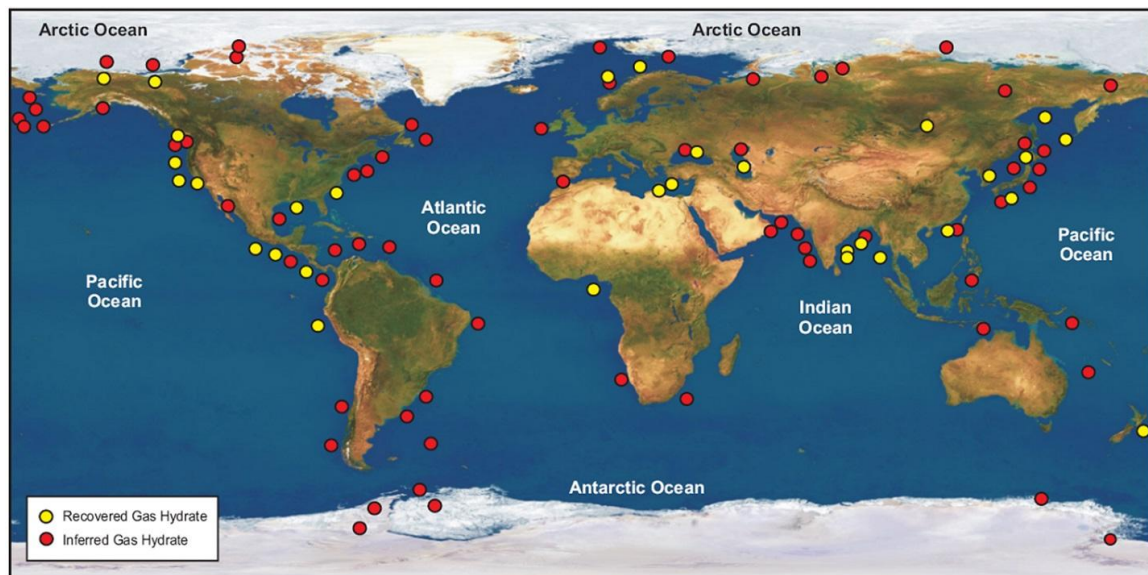


Figure 2.1: Worldwide map of recovered and inferred gas hydrates, from Council of Canadian Academies (2008). This map includes both permafrost and deepwater marine locations.

Methane hydrates have been studied for decades for various economic and environmental reasons. It has been estimated that hydrate deposits contain 1600-2000 Gt

(Archer et al., 2008) and 500-3500 Gt of carbon (Milkov, 2004), almost twice the amount of carbon held in all other fossil fuels combined. These reservoirs make methane hydrates a potential source of energy (Collett, 2002; Max et al., 2006). At standard temperature and pressure conditions, a cubic meter of methane hydrate dissociates into roughly 0.8 m<sup>3</sup> of water and greater than 160 m<sup>3</sup> of methane (Bahadori, 2014). Therefore, methane hydrates are a potential energy resource that could represent an important future resource as oil reserves become depleted. However, due to technical challenges, methane hydrate is not currently being exploited for energy.

There are environmental concerns regarding hydrates as well. A study by Dickens et al. (1995) suggested that methane hydrate caused a major climate excursion in the late Paleocene. An increase of ocean temperature or a drop in sea level resulting in a decrease in pressure can cause hydrate to dissociate and emit methane into both ocean and atmosphere and change the climate in both environments. Archer et al. (2008) proposed that hydrates may affect climate in the future as well. Similarly, gas hydrates may have the potential to generate submarine slope failures as well. The slope failures may occur when there is a disturbance within gas hydrate stability zones (GHSZs) causing the shear strength of the formation to decrease as hydrates dissociate into water and free gas. Modeling results of Mienert et al. (2005) suggest that the reduced hydrate stability conditions could have contributed to the slope failure of the Storegga slide offshore Norway.

There are three different crystal structures for hydrates: structure I, structure II, and structure H. Due to different chemical and physical properties, structure I and structure II gas hydrates may have different expressions in seismic records. However, structure I is the most common crystal structure in natural methane hydrates (Kvenvolden, 1993; Sloan, 1998).

### 2.1.2: Methane Hydrate Stability and Occurrences

The crystal structure of methane hydrate is stable within a certain range of pressure and temperature. For illustration, phase diagrams are used to present the relationship between pressure and temperature under which hydrates are stable.

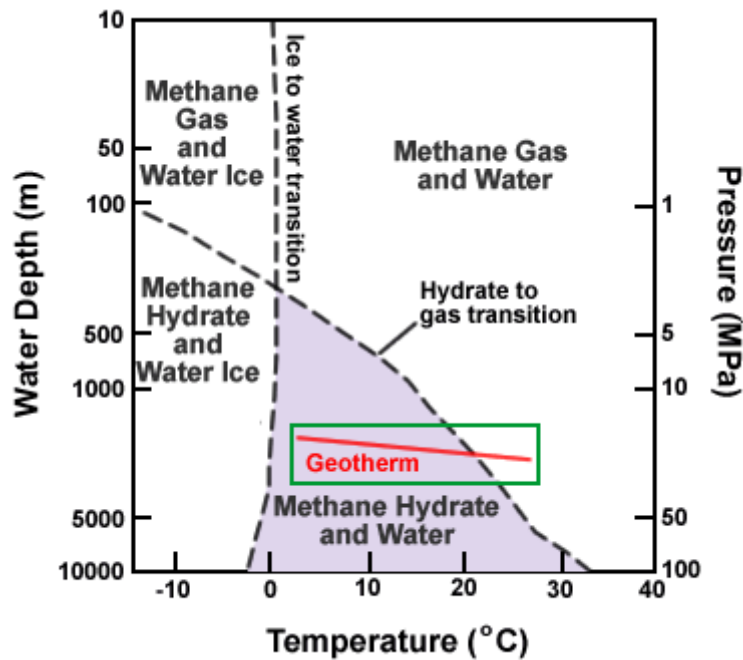


Figure 2.2: Phase diagram for methane hydrate. This figure illustrates how pressure and temperature play a role on the stability of methane hydrates. Factors such as salinity and pore sizes also affect the stability of methane hydrate. Figure from NOAA Ocean Explorer 2010.

Figure 2.2 allows us to study the physical condition of the methane hydrates, as it shows the boundary between melting and solidifying of the fluids. For a given pressure and temperature, there will be a unique set of phase equilibria. The dashed lines separate the phase equilibrium between the following:

1. Methane gas and water ice with methane hydrate and water ice
2. Methane hydrate and water ice with methane hydrate and water

3. Methane hydrate and water with methane gas and water

4. Methane gas and water with methane gas and water ice

The most important lines are the hydrate to gas transition (dashed line), and the geotherm line drawn in red (geotherm represents the temperature in sediments below the sea floor). Above the hydrate to gas transition line, no hydrate is formed. The temperature of the layers below the sea floor begins to increase starting from 3-4°C as depth below the seafloor increases. When the geotherm line crosses the hydrate to gas transition, where the temperature is too high for methane hydrates to exist, hydrates melt to free gas. This simply implies that the free gas is overlain by the methane hydrate and that the interface between these boundaries lies parallel to the seafloor. In seismic data, this boundary has a unique signature. This feature is called bottom-simulating reflection. Figure 2.3 below shows an example of the bottom-simulating reflection from the Blake Ridge offshore of South Carolina. The amount of free gas is an important factor for this signature to be observed in seismic data. Further discussions regarding bottom-simulating reflections are given in section 2.3.1.

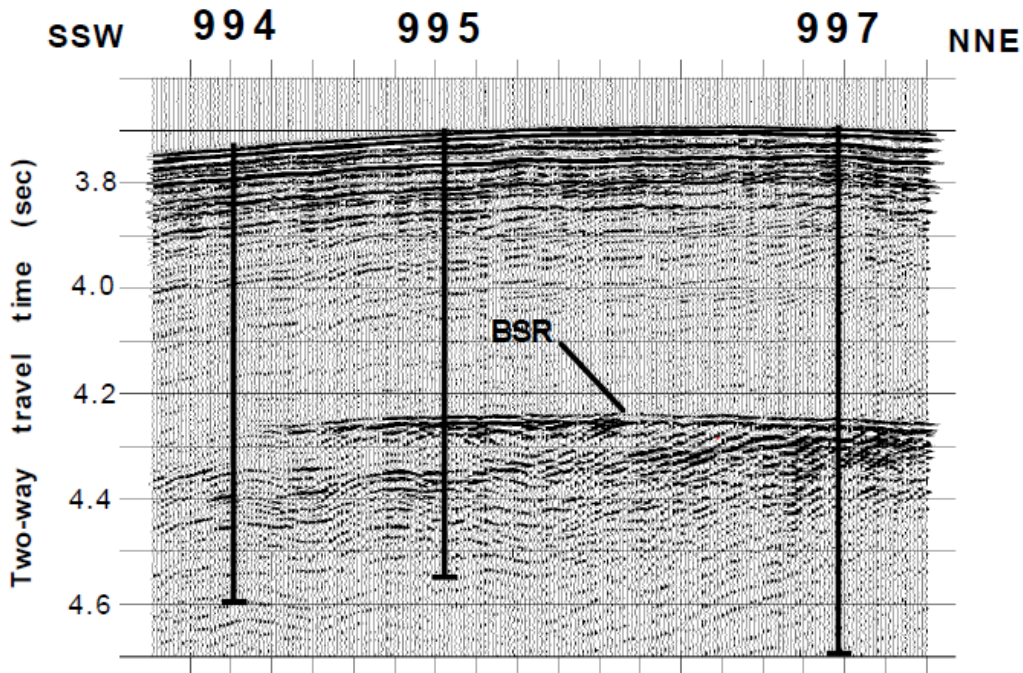


Figure 2.3: An example of predominant signature of a bottom-simulating reflection from Blake Ridge in off-shore of South Carolina. Bottom-simulating reflections are not always as clearly visible. Figure from Paull and Matsumoto (2000).

### 2.1.3: Structures of Gas Hydrate

Gas hydrates formed from natural gases may occur in one of the three structures: structure I (body-centered cubic), structure II (diamond lattice), and structure H (hexagonal).

Unlike structure H which was identified a decade ago, structures I and II have been known for many years and have simpler structures comparably. Five kinds of hydrate cages which have been found to exist in all three natural structures are illustrated in Figure 2.4. Structure I and II crystallize in a cubic arrangement, whereas structure H crystallizes in a hexagonal arrangement. Water molecules are held together in a tetrahedral arrangement by hydrogen bonds in gas hydrate crystal lattices (Sloan, 1998).

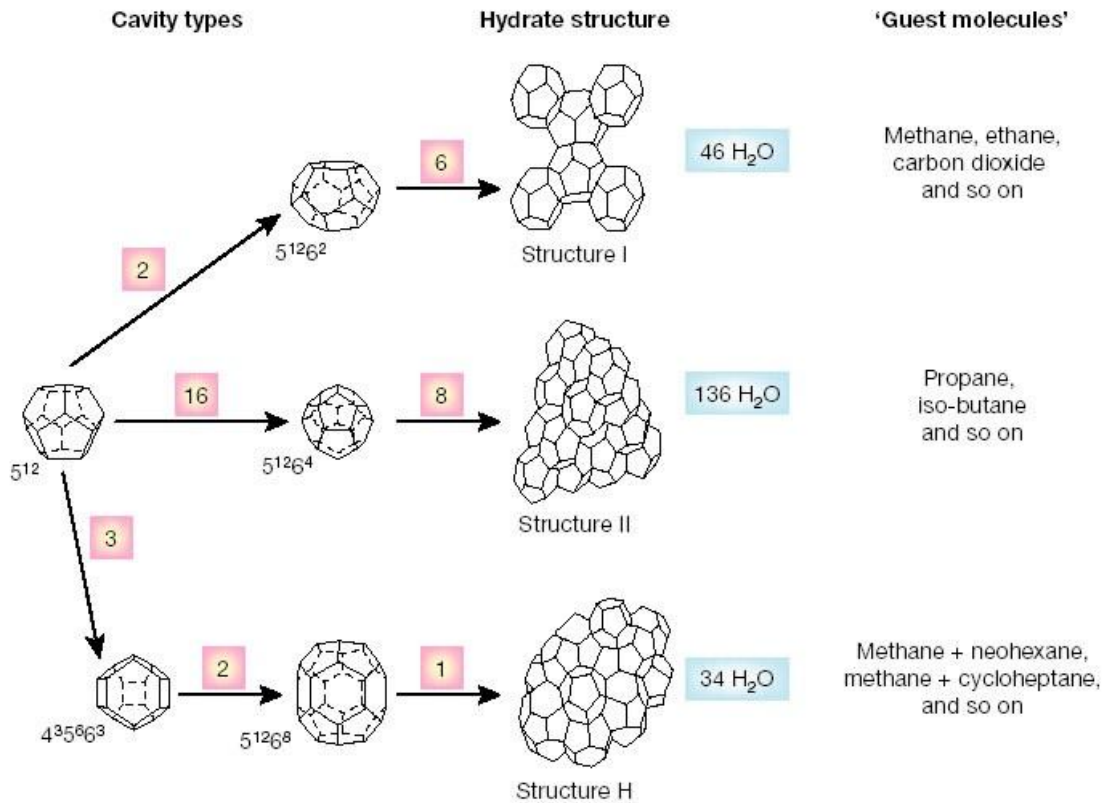


Figure 2.4: Three hydrate unit crystals and three natural structures of gas hydrates (Sloan, 1998).

Structure I has the simplest and most common hydrate structure. This structure has 8 gas molecules. These 8 gas molecules are associated with 46 water molecules. The number of water molecules is to be found from a theoretical equation of  $5.75x$ , where  $x$  is the number of hydrate molecules (Sloan, 1998). Typical gas molecules found in Structure I are  $\text{CO}_2$  and  $\text{CH}_4$ .

Structure II hydrate is more complicated than structure I. This structure has 24 gas molecules and 136 water molecules. The common gas molecules in the Structure II are nitrogen, propane, and isobutene.

Structure H hydrate is associated with 34 water molecules. Structure H needs two kinds of gases including a large structure H forming molecule, which is not commonly

found, while structure I and II hydrates can come out from a single gas (Sloan, 1998). Structure H hydrate do exist in nature; however, properties for this type of hydrate are not completely known.

#### **2.1.4: Bottom-Simulating Reflection**

Marine gas hydrates are stable in the upper few hundreds of meters below the seafloor under conditions of low temperature and high pressure. Typically the transition from hydrate-bearing sediments to gas-bearing sediments is assumed to occur at a discrete horizon where the thermodynamically favored phase switches from hydrate to gas. This horizon produces a characteristic seismic reflection referred to as the bottom-simulating reflection (BSR). However, in sediments with a distribution of pore sizes, the gas and hydrate phases can coexist in pores of different sizes, giving rise to a zone of three-phase equilibrium. This three-phase zone causes the BSR to have distinct characteristics that differ from those observed with a discrete phase boundary (Tréhu et al., 2006; Waite et al., 2007).

The work by Ecker and Lumley (1994) showed that the BSR separates hydrate bearing sediments from the underlying sediments containing free gas. Therefore, the BSR marks the boundary between sediments containing gas hydrate above and free gas below. When gas is present in the formation, there is a large decrease in the bulk density and bulk modulus of the formation. This transition from hydrate above to gas-hydrate mixture below is the main reasons for the presence of the BSRs. BSRs are high-amplitude, reverse-polarity events.

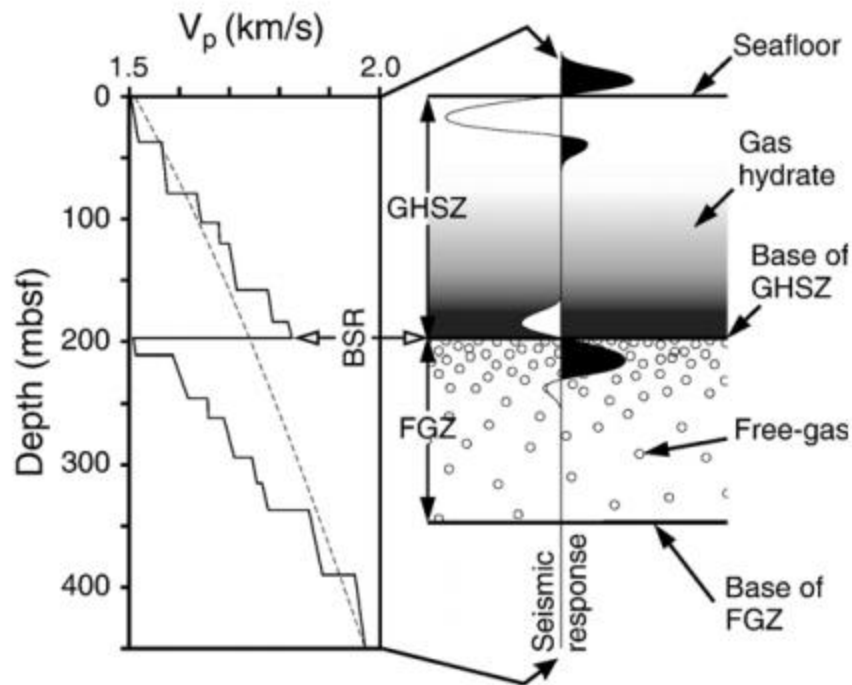


Figure 2.5: Illustration of a submarine sedimentary section containing gas hydrate (above) and free gas (below) the BSR (Haacke et al., 2007)

The BSR is characterized by amplitudes which are increasingly negative with increasing incidence angle of the seismic wave, amplitude versus offset (AVO). This effect can be explained (schematically shown in Figure 2.5) by P-wave velocity above the BSR being larger than that below the BSR, S-wave velocity above the BSR being lower than that below the BSR, and density above the BSR being larger than that below the BSR. It has to be mentioned that gas hydrate can occur without a BSR as well; however, the controls on its formation are not well understood (Haacke et al., 2007). It is to our interest to better understand the prominent signature feature, to model the seismic velocities, and to determine seismic properties of 3-phase zone.

Two of the main classes of the BSRs are the base of gas hydrate bearing sediments, and the opal-A/opal-CT phase boundary (Berndt et al., 2004). Figure 2.5

illustrates gas hydrate bearing sediments where the BSR is a result of the change from high-velocity gas hydrate-bearing sediments above to low-velocity gas-bearing sediments below. This change in velocity creates a sharp acoustic impedance contrast between the layers (Bryan, 1974; Holbrook et al., 1996). This will result in high seismic amplitude that has a reverse polarity reflection compared to the seafloor reflection. The opal-A to opal-CT transition is as a result of dissolution and diagenesis of biogenic silica (Murata and Nakata 1974). Strong positive polarity is produced as the density between the interfaces increase (Lee et al., 2003).

## **2.2: FIELD LOCATIONS**

### **2.2.1: Blake Ridge**

Leg 164 Hole 995B is located in Blake Ridge offshore of South Carolina. This well was drilled by Ocean Drilling Program (ODP) in late 1995. Figure 2.3 in section 2.1.2 shows the BSR in Blake Ridge.

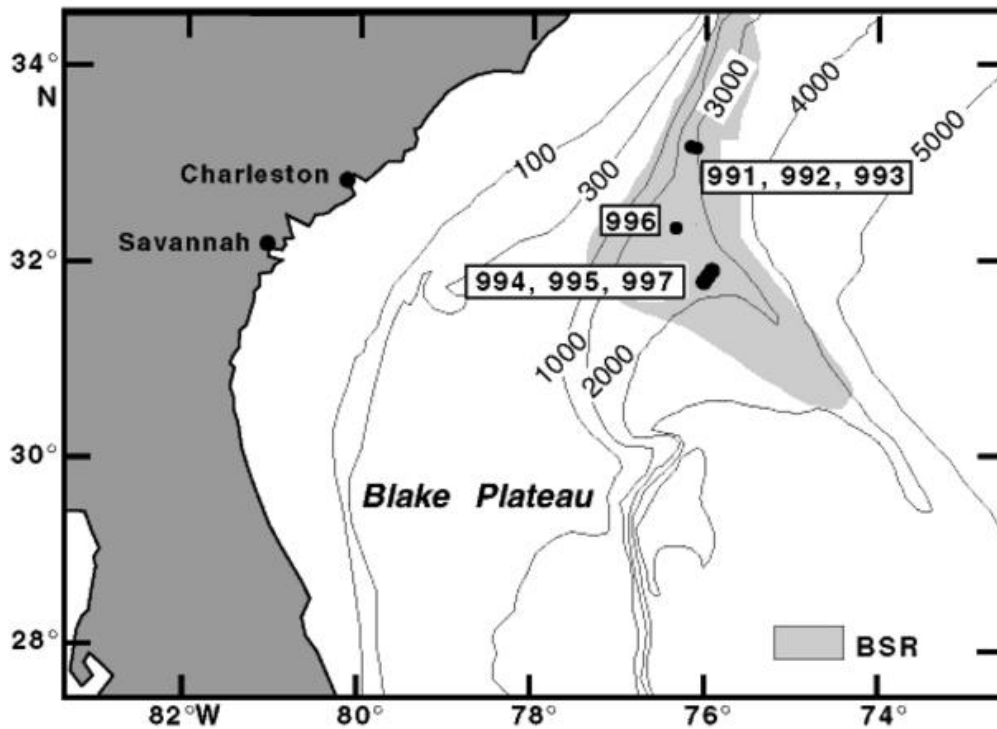


Figure 2.6: Location map of Leg 164 sites on the southeastern North American continental margin. (Note: contours are in meters). Blake Ridge's Hole 995B is located in center part of Blake Ridge with coordinates: 31° 48.217' N, 75° 31.336' W with hole depth of 2776.9 meters/9110.6 feet below sea level (Paull et al., 1996).

### 2.2.2: Walker Ridge

The Walker Ridge 313H well is located in the northwest portion of the Walker Ridge area, northern Gulf of Mexico. This well was the second well drilled in the Terrebonne Basin, a salt withdrawal mini-basin, during the 2009 Gulf of Mexico Gas Hydrate Joint Industry Project Leg II (Collett et al., 2012; Frye et al., 2012).

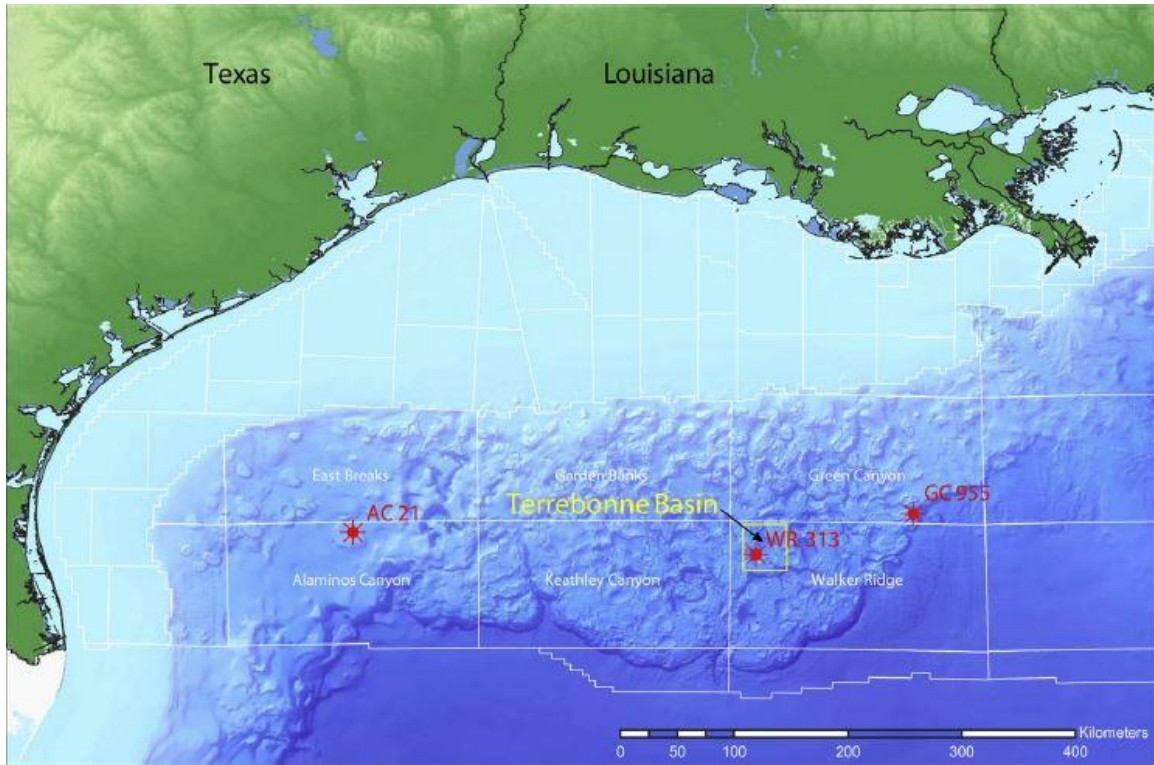


Figure 2.7: Northern Gulf of Mexico's Bathymetric relief map (Frye et al., 2012). Walker Ridge's 313H well is located at northwest part of Walker Ridge region with coordinates: 26° 39' 44.8482" N, 91° 40' 33.7467" W with water depth of 1966.3 meters/6451 feet below sea level and hole depth of 996.1 meters/3268 feet below sea floor (Collett et al., 2012)

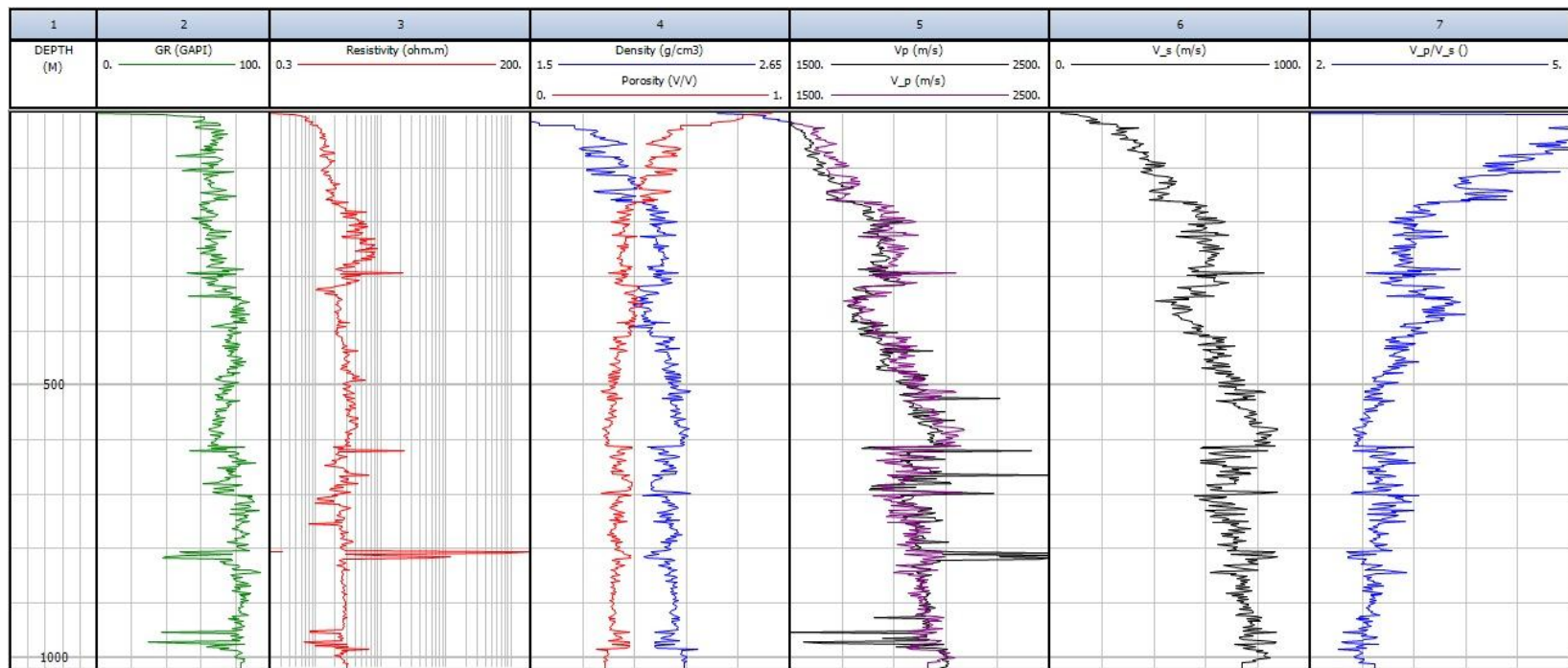


Figure 2.8: Presents some of the raw (Gamma ray, resistivity, density, and V<sub>p</sub>/compressional velocity), calibrated (Porosity), and calculated (V<sub>p</sub> and V<sub>s</sub>/shear velocity) data from WR 313H. All calculations are explained in the section 2.3.

### 2.3: ROCK-PHYSICS MODELS

There are two models that may be used to describe the acoustic behavior of hydrate-bearing sediments. The first model, the contact-cement model, assumes that hydrate has cemented the grain contacts as shown in Figure 2.9A below. In this model, hydrate acts similarly to cement, giving additional mechanical strength to the sediments. Using this model will greatly increase the elastic moduli of the rock frame with the addition of hydrate. The second model, the no-contact-cement model (Figure 2.9B), assumes that the hydrate is deposited away from grain contacts. In this model, hydrate is generated within the pore fluid and the elastic moduli of the sediment frame are not affected by its presence. These physical rock models link the elastic wave velocities in high-porosity sediments to porosity, density, effective pressure, mineralogy and fluid saturation.

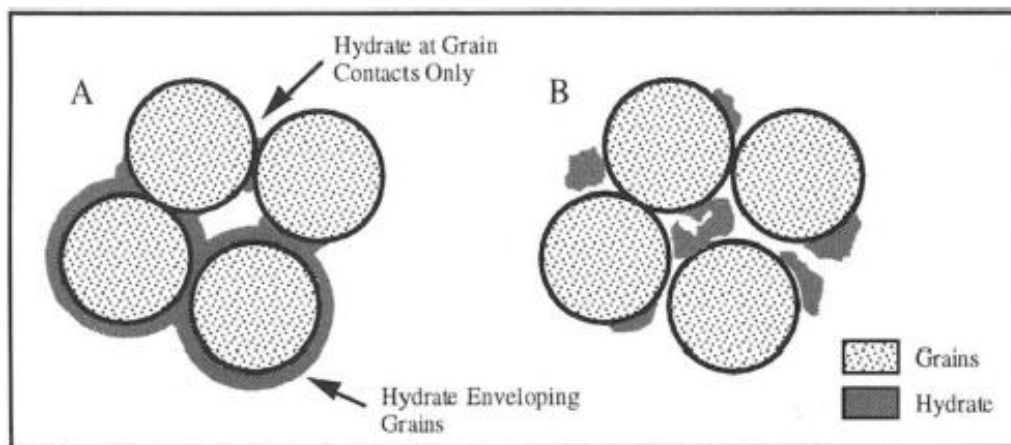


Figure 2.9: Model A, the contact-cement model, assumes that hydrate cements the grain evenly. Model B, the no-contact-cement model for hydrate deposition among the grains (Ecker et al.,1998).

Ecker et al. (1998) concluded that hydrate does not cement the grain contacts as only the no-contact-cement model could qualitatively reproduce the observed amplitude versus offset response. Since no contact-cement model best represents the hydrate deposition among grains, this model makes rock physics analysis for next steps much simpler.

The bulk and shear moduli,  $K$  and  $G$  respectively, can be used to directly relate changes in lithology and hydrate saturation to mechanical properties. These two parameters are related to the acoustic velocities by

$$G = \rho_B V_s^2, \quad (2.1)$$

$$K = \rho_B \left( V_p^2 - \frac{4}{3} V_s^2 \right), \quad (2.2)$$

where  $\rho$  is density of the formation,  $V_p$  is compressional velocity, and  $V_s$  is shear velocity.

The acoustic velocities can be determined by rearranging Equations (2.1) and (2.2) as

$$V_p = \sqrt{\frac{K_{sat} + \frac{4}{3} G_{sat}}{\rho_B}}, \quad (2.3)$$

$$V_s = \sqrt{\frac{G_{sat}}{\rho_B}}, \quad (2.4)$$

$$\rho_B = (1 - \Phi) \rho_s + \Phi \rho_f, \quad (2.5)$$

where  $\Phi$  is porosity,  $\rho_s$  is the bulk density of the solid phase and  $\rho_f$  is the density of the pore fluid.

Gassmann's (1951) equations express the bulk and shear modulus as functions of the elastic moduli of rock minerals and fluids and their relative abundances. These equations may be used to calculate the acoustic velocity changes as a result of substitution of the fluid saturations in pore space. Therefore, these equations provide a framework for describing the changes in elastic properties as hydrate or gas saturation change.

Gassmann's equations express the saturated bulk and shear moduli  $K_{sat}$  and  $G_{sat}$  as

$$K_{sat} = K \frac{\phi K_{dry} - \frac{(1 + \phi)K_f K_{dry}}{K} + K_f}{(1 - \phi)K_f + \phi K - \frac{K_f K_{dry}}{K}}, \quad (2.6)$$

$$G_{sat} = G_{dry}, \quad (2.7)$$

where  $K$  is the bulk modulus of the matrix/rock (solid mineral grains),  $K_f$  is the bulk modulus of the pore fluid (Section 2.3.1),  $K_{dry}$  and  $G_{dry}$  are the dry bulk and shear moduli of the rock (Section 2.3.2), and  $\phi$  is the void volume fraction of the formation known as porosity. The shear modulus is independent of fluid saturation (Berryman, 1999). The modified Hashin-Shtrikman-Hertz-Mindlin theory (Dvorkin et al., 1998) can be used to find the bulk and shear moduli of the dry frame ( $K_{dry}$  and  $G_{dry}$ ). This theory first calculates the effective bulk and shear moduli at a critical porosity using the Hertz-Mindlin theory (Mindlin, 1949). Critical porosity ( $\phi_c$ ) can vary between 36% and 40%; these two values represent the porosity of a random dense pack of spherical grains. The critical porosity separates the mechanical and acoustic behavior into two distinct regions (Nur et al., 1995): for porosities lower than  $\phi_c$ , the mineral grains are load bearing, while

for porosities greater than  $\phi_c$ , the sediment becomes a suspension, with the fluid phase becoming load-bearing. The effective moduli at the critical porosity are given by

$$K_{HM} = \left[ \frac{G^2 n^2 (1 - \phi_c)^2}{18\pi^2 (1 - \nu)^2} P \right]^{\frac{1}{3}}, \quad (2.8)$$

$$G_{HM} = \frac{5 - 4\nu}{5(2 - \nu)} \left[ \frac{3G^2 n^2 (1 - \phi_c)^2}{2\pi^2 (1 - \nu)^2} P \right]^{\frac{1}{3}}, \quad (2.9)$$

where  $n$  is the average number of contacts per grain that varies between 4 and 10 depending on compaction and consolidation. For relatively compacted and consolidated formations value this value is taken to be 8.5 (Murphy, 1982). A value of 9 can be used for close packing.  $\nu$  is the Poisson's ratio of the mineral phase calculated from  $K$  and  $G$  as following:

$$\nu = \frac{3K - 2G}{2(3K + G)}, \quad (2.10)$$

If the sediment rock consists of a mixed mineralogy, the bulk and shear moduli  $K$  and  $G$  of the rock can be determined using a Hill's average formula:

$$K = \frac{1}{2} * \left[ \sum_{i=1}^m f_i K_i + \left( \sum_{i=1}^m \frac{f_i}{K_i} \right)^{-1} \right], \quad (2.11)$$

$$G = \frac{1}{2} * \left[ \sum_{i=1}^m f_i G_i + \left( \sum_{i=1}^m \frac{f_i}{G_i} \right)^{-1} \right], \quad (2.12)$$

where  $m$  is the number of different mineral components,  $f_i$  is the volumetric fraction of the  $i^{th}$  component in the rock, and  $K_i$  and  $G_i$  are the bulk and shear moduli of the  $i^{th}$  component, respectively. An alternate approach to Hill's average may be employed by

expressing the elastic moduli of the grains as a linear combination of two end members whose volume fractions are defined by the gamma ray log (e.g., Guerin et al., 1999).

Guérin et al. (1999) uses the Voigt-Reuss-Hill average of the grain moduli of the two main mineral phases of sand ( $K_s$  and  $G_s$ ) and clay ( $K_c$  and  $G_c$ ). The grain bulk modulus can be calculated by

$$K = \frac{1}{2} \left[ \gamma K_c + (1 - \gamma) K_s + \frac{K_s K_c}{K_s \gamma + K_c (1 - \gamma)} \right], \quad (2.13)$$

$$G = \frac{1}{2} \left[ \gamma G_c + (1 - \gamma) G_s + \frac{G_s G_c}{G_s \gamma + G_c (1 - \gamma)} \right], \quad (2.14)$$

where  $\gamma$  is normalized gamma ray values and it is used to define the clay mineral percentage in the sediments. The grain moduli of  $K_s$  and  $K_c$  are in Appendix, Table 1.

$P$  in Equation 2.15, is the effective pressure applied to grain pack and is calculated from:

$$P = (1 - \phi)(\rho_s - \rho_f)gh, \quad (2.15)$$

where  $\rho_f$  and  $\rho_s$  are the densities of the fluid and solid phase respectively;  $h$  is the depth below seafloor; and  $g$  is the acceleration due to gravity.

### 2.3.1: Bulk Modulus of Pore Fluid

#### *Sediments without Gas Hydrate*

$K_f$  is identical to the bulk modulus of water, in the case of purely brine-saturated sediments. If the sediment is homogeneously saturated with gas,  $K_f$  becomes an isostress average of water ( $K_w$ ) and gas ( $K_g$ ) at saturation  $S_w$ . It can be found by following equation:

$$K_f = \left[ \frac{S_w}{K_w} + \left( \frac{1 - S_w}{K_g} \right) \right]^{-1}, \quad (2.16)$$

#### *Sediments with Gas Hydrate*

As mentioned before, the no-contact-cement model assumes that the hydrate is deposited away from grain contacts. Hydrate is generated within the pore fluid and the elastic properties of the sediment are not affected or subjected to change. Similarly to the sediment without gas hydrate, the pore fluid will consist of a mixture of brine, hydrate, and gas. Therefore, for the case of hydrate being part of pore fluid, the bulk modulus of the fluid is the isostress average of water, hydrate, and gas. The bulk modulus of the fluid is calculated from the following equation:

$$K_f = \left[ \frac{S_w}{K_w} + \frac{S_h}{K_h} + \frac{S_g}{K_s} \right]^{-1}, \quad (2.17)$$

### 2.3.2: Dry Bulk and Shear Moduli

#### *Hashin-Shtrikman Model*

Modified Hashin-Shtrikman upper and lower bound is then used to calculate the dry moduli of the solid phase for porosities above and below the critical porosity (Dvorkin and Nur, 1996; Ecker et al., 1996).

If the porosity is below the critical porosity of 40%, the dry moduli can be calculated as

$$K_{dry} = \left[ \frac{\frac{\phi}{\phi_c}}{K_{HM} + \frac{4}{3}G_{HM}} + \frac{1 - \frac{\phi}{\phi_c}}{K + \frac{4}{3}G_{HM}} \right]^{-1} - \frac{4}{3}G_{HM}, \quad (2.18)$$

$$G_{dry} = \left[ \frac{\frac{\phi}{\phi_c}}{G_{HM} + Z} + \frac{1 - \frac{\phi}{\phi_c}}{G + Z} \right]^{-1} - Z, \quad (2.19)$$

$$Z = \frac{G_{HM}}{6} \left[ \frac{9K_{HM} + 8G_{HM}}{K_{HM} + 2G_{HM}} \right], \quad (2.20)$$

If the porosity is above the critical porosity of 40%, the dry moduli can be calculated as

$$K_{dry} = \left[ \frac{\frac{1 - \phi}{1 - \phi_c}}{K_{HM} + \frac{4}{3}G_{HM}} + \frac{1 - \phi}{1 - \phi_c} \frac{1}{\frac{4}{3}G_{HM}} \right]^{-1} - \frac{4}{3}G_{HM}, \quad (2.21)$$

$$G_{dry} = \left[ \frac{\frac{1 - \phi}{1 - \phi_c}}{G_{HM} + Z} + \frac{1 - \phi}{1 - \phi_c} \frac{1}{Z} \right]^{-1} - Z, \quad (2.22)$$

### **Wood Model**

The model derived by Wood (1941) considers the mechanical behavior of unconsolidated sediments as particles in suspension. The dry bulk modulus by Wood is determined as

$$K_{dry-Wood} = \frac{KK_f}{\phi K + K_f(1 - \phi)}, \quad (2.23)$$

where  $K$  is the weighted average of the compressibility of the grain aggregate, and  $K_f$  is the weighted average of the compressibility of the pore fluid.

### ***Hamilton Model***

Hamilton (1971) established a relationship between the dry bulk modulus and the porosity of marine sediments. He defined two different relationships for fine sand and silt-clay as following:

$$\log(K_{dry}(*10^{-9}Pa)) = 1.7093 - 4.25391\phi, \quad (2.24)$$

$$\log(K_{dry}(*10^{-9}Pa)) = 1.7358 - 4.25075\phi, \quad (2.25)$$

It has to be mentioned that the first terms on the right of these two equations represent the logarithm of the grain bulk modulus  $K$ , which is equal to the dry bulk modulus at zero porosity. Furthermore, these two distinct relationships can be defined to a single formula for elastic sediments:

$$\log(K_{dry}) = \log(K) - 4.25\phi \quad (2.26)$$

or

$$\log\left(\frac{K_{dry}}{K}\right) = -4.25\phi, \quad (2.27)$$

Solving for  $K_{dry}$  for more ease of use, we would have the following:

$$K_{dry} = K * 10^{-4.25\phi}, \quad (2.28)$$

This generalization ensures that the frame bulk modulus equals the grain bulk modulus at  $\phi = 0$  for any value of the aggregate grain modulus. Furthermore, combination of Hamilton's and Gassmann's equation is referred as the Gassmann-Hamilton Model.

### 2.3.3: Sediments Mineralogy and Calculation

Mineralogy takes an important role in the properties of sediment, and therefore it is required to have knowledge the mineralogy of the sediments. Different sites around the world have different mineralogy, which may change the approaches for to a solution. For example, Ecker et al. (2000) used a homogeneous model where formation consisted of 60% clay, 35% calcite, and 5% quartz for all layers. For this study, since the sediments at Walker Ridge are dominantly clay and quartz, a normalized gamma ray was used to calculated the bulk and shear moduli of the formation. This means that every single depth in the well has its own unique set of shear and bulk moduli.

Substance	Bulk Modulus (Gpa)	Shear Modulus (Gpa)	Density (g/cm3)
Calcite	76.8	32	2.71
Clay	20.9	6.85	2.58
Quartz	36	45	2.65
Brine	2.5	0	1.032
Pure Hydrate	5.6	2.4	0.9
Gas	0.1	0	0.235

Table 2.1: Calculation parameters used in this study (Ecker et al., 2000).

### 2.4: SYNTHETIC SEISMOGRAMS

Modeling a seismic response of a rock that is saturated with different fluids is one of the fundamental tasks in rock physics. A synthetic seismogram allows us to observe how a seismic wavelet would travel through a formation that has different petrophysical properties such as porosity, fluids, and density. Furthermore, fluid substitution is directly reflected on the AVO responses. Changes in petrophysical properties will change the acoustic velocities and therefore changes the seismic amplitudes (Stewart et al., 1984).

Synthetic seismograms are generated by convolution of the reflection coefficient at an interface with a seismic wavelet. The reflection coefficient is the ratio of amplitude of the reflected wave to incident wave and is expressed as

$$R = \frac{Z_2 - Z_1}{Z_2 + Z_1}, \quad (2.29)$$

where  $Z_2$  is the acoustic impedance of the formation below and  $Z_1$  is the acoustic impedance of the formation above. Acoustic impedance is the product of density and compressional velocity:

$$Z = \rho V_p, \quad (2.30)$$

Equation 2.29 can be rewritten as

$$R = \frac{\rho_2 V_2 - \rho_1 V_1}{\rho_2 V_2 + \rho_1 V_1}, \quad (2.31)$$

Convolution is a mathematical operation where two functions, in this case the reflection coefficient and wavelet, are summed together to yield a third function to present a process of linear filtering. The convolution of two functions, a filter  $f(t)$  and a time-series  $x(t)$ , in the mathematical form is expressed as

$$y(t) = (f * g)(t) = \int f(t - T)g(T)dT, \quad (2.32)$$

In area of this study, convolution is a product of the Fourier transform of the two functions with addition of noise and is expressed as

$$T(t) = R(t) * \omega(t) + n(t), \quad (2.33)$$

where  $T$  is seismic trace,  $R$  is reflection coefficient,  $\omega$  is wavelet, and  $n$  is noise. A physical interpretation of the convolution can be best presented graphically as shown in the figure below.

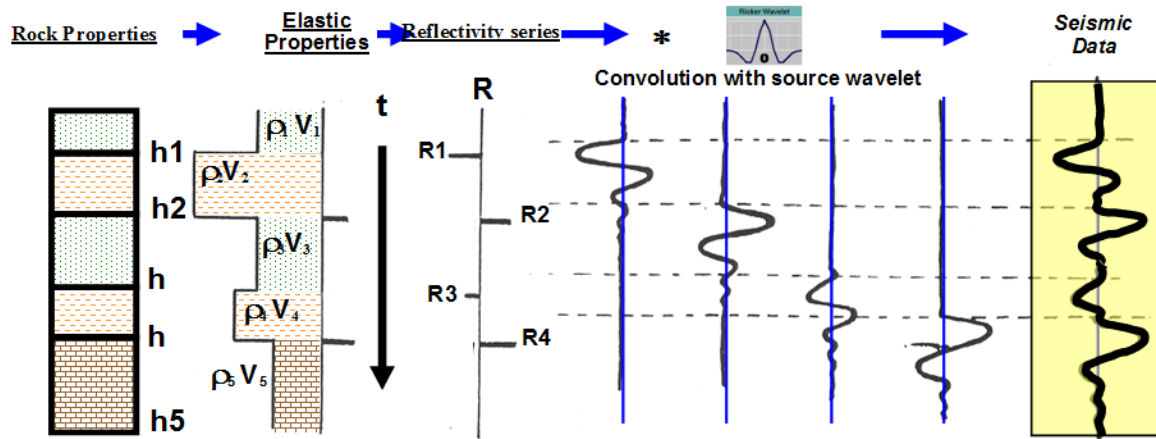


Figure 2.10: Graphical presentation of convolution process in creation of synthetic seismogram (Interactive Petrophysics, 2014).

Synthetic seismograms allow seismic scale study of petrophysical properties of formations. This opens feasibility in AVO studies when performing fluid substitution as the reflection coefficient depends on the angle of incidence of the seismic wave. The reflection coefficient can be estimated at a given angle of incident using the Zoeppritz equations (Zoeppritz, 1912).

Rutherford and Williams (1989) first presented AVO variations in a gas sand and introduced the first three different classes of AVO. Later Castagna et al. (1998) introduced Class IV that was not discussed by Rutherford and Williams. These classes became the industry standard and are follow as

Class I- High impedance sand

Class II- Near zero impedance contrast sand

Class III- Low impedance sand with increasing amplitude magnitude with offset

Class IV- Low impedance with decreasing amplitude magnitude with offset

BSRs are typically Class III or Class IV AVO anomalies (Carcione and Tinivella, 2000).

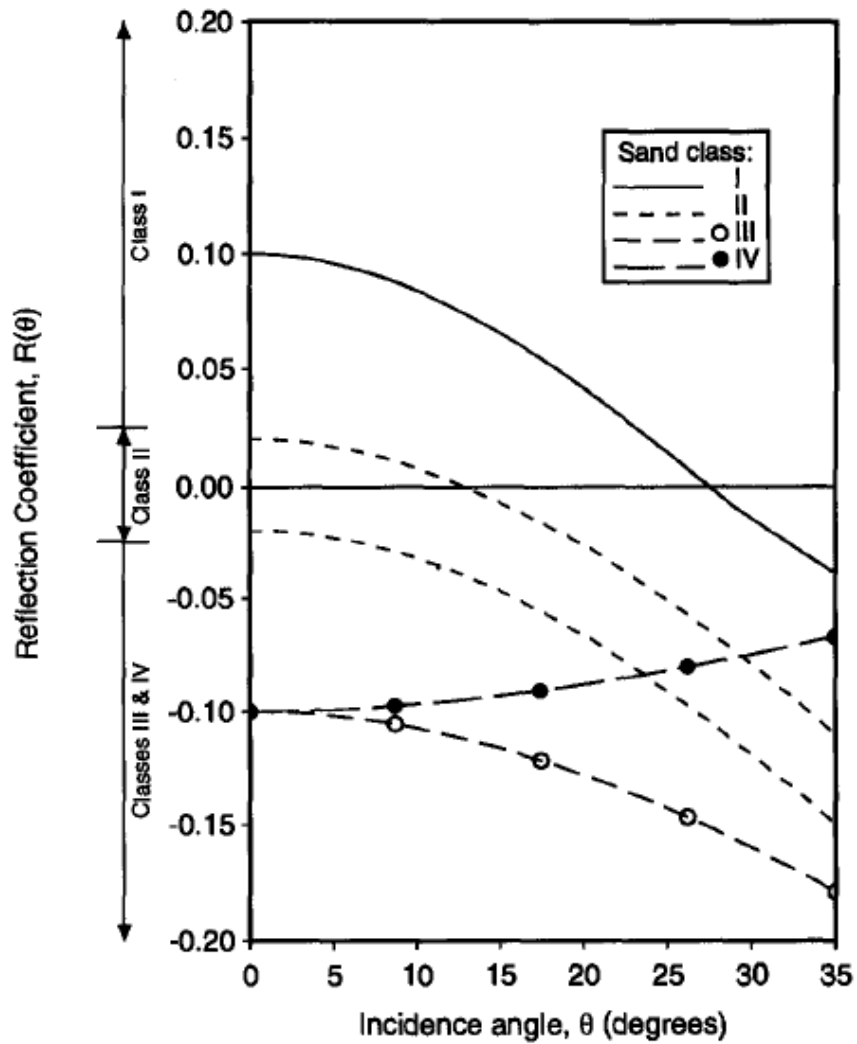


Figure 2.11: AVO's 4 classification reference guide (Castagna et al., 1998).

## **Chapter 3: Methodology**

### **3.1: OVERVIEW**

This chapter presents an overview of the data used in this study, and describes the steps applied to the data before creating the synthetic seismograms. Preparation of the data includes choosing the most accurate rock physics model, the right number of contacts per grain lithology, acoustic velocities, travel time, and preparation of the seismic wavelet. After preparation of the data, Interactive Petrophysics software is introduced and procedures for its use are described.

### **3.2: DRY MODULUS MODELS**

In Chapter 2, we introduced models by Hashin-Shtrikman, Wood, and Hamilton in order to find the dry modulus of the formation. Wood and Hamilton's models were used by Guerin et al. (1999) as a reference to compare the bulk modulus with the well-logging data. A reproduced figure for bulk modulus from ODP Leg 164 Hole 995B at Blake Ridge from Guerin et al. (1999) is presented in Figure 3.1.

Guerin et al. (1999) divided this log into four units with distinct signatures: (I) above ~180 meters below sea floor (mbsf), (II) between ~180 and ~440 mbsf, (III) between ~440 and ~520 mbsf, and (IV) below ~520 mbsf. The pore fluids for these units are interpreted as follows:

Unit (I): Water

Unit (II): Water and hydrate

Unit (III): Water, hydrate, and minimal amount of gas.

Unit (IV): Water and gas.

Unit (III) corresponds to the decrease in compressional velocity, which is due to the presence of gas. Since hydrates are present in this unit, it is difficult to observe that

the bulk modulus is reduced. Unit (IV), however, is a free gas zone and contains no hydrates. As a result, it is easy to observe that the bulk modulus drops significantly. However, the Wood and Hamilton models do not reflect or represent the actual well-logging data for layers above the BSR (Unit II), and when layers of free gas were encountered (Unit IV).

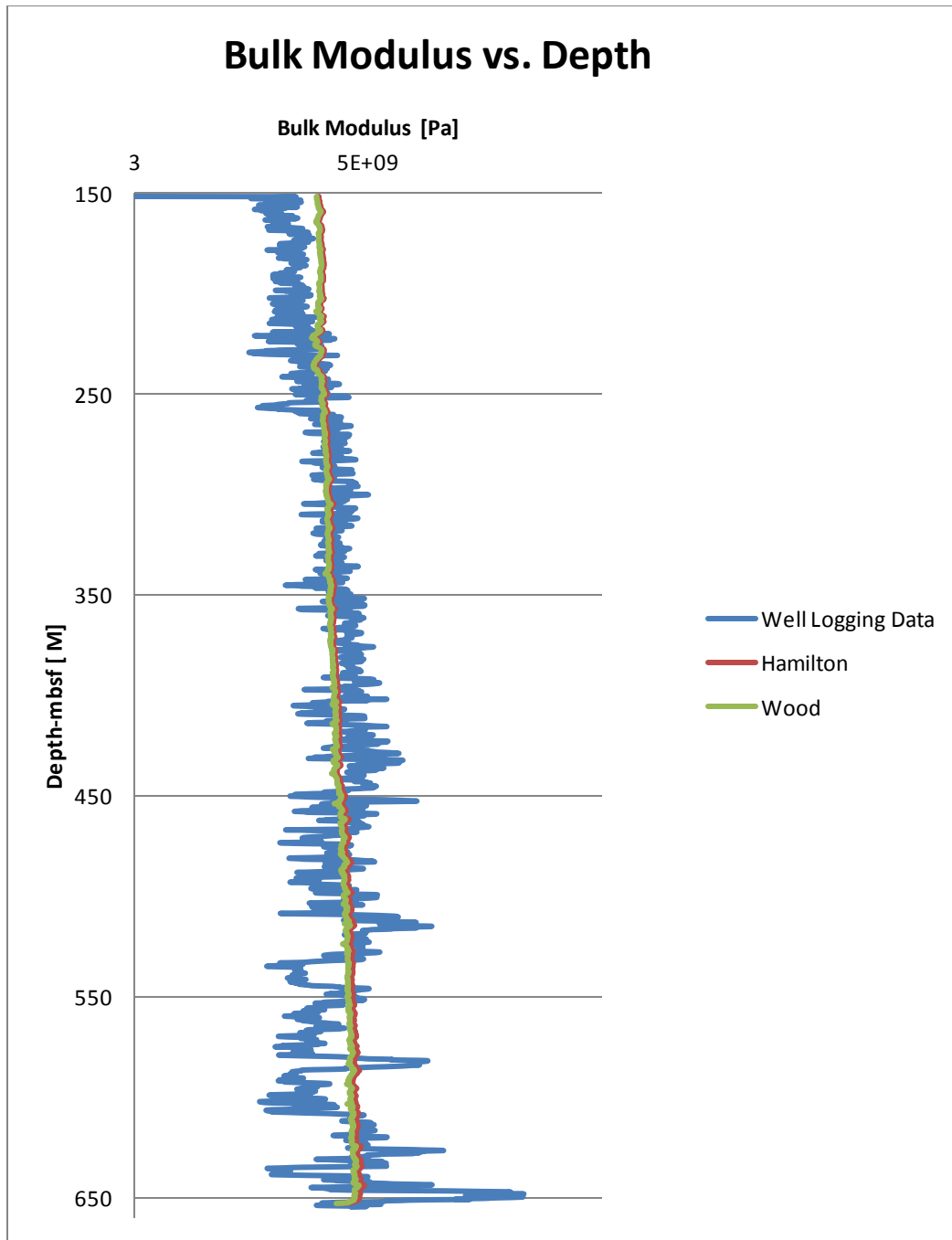


Figure 3.1: Reproduced figure from Guerin et al. (1999) for Blake Ridge ODP Leg 164 Hole 995B. Above ~440 mbsf and below ~520 mbsf the Wood and Hamilton model do not reflect or match the well-logging data. Equation (2.2) was used to find the bulk modulus for well-logging data.

Ecker et al. (2000) used the Hashin-Shtrikman approach to find the dry modulus. This model correlates with the actual data to a great extent if the number of contacts per grain is chosen correctly (described in section 3.2.2). Moreover, when encountering layers saturated with hydrates and gas, a reduction of the bulk modulus can be observed. Therefore, this study uses Hashin-Shtrikman to find the dry modulus.

### **3.3: NUMBER OF CONTACTS PER GRAIN**

The number of contacts per grain plays an important role as it significantly affects the elastic properties of the sediments. In this study,  $n$  is the average number of contacts per grain and can vary between 4 and 10 depending on the compaction and consolidation of the formation. For young sediments that are yet to be compacted and consolidated, this value is on the lower end of this range, while in compacted and consolidated formations a value of 8.5 is suggested by Murphy (1982).

In this study, multiple models were created and compared to the actual well-logging data. We compared the compressional velocity from well-logging data with the models created by a different number of contacts per grain (This is assuming that pores medium is saturated only with water). Compressional velocities were determined using the equation (2.3) presented in Chapter 2. Figure 3.2, 3.3, and 3.4 illustrate how the average number of contacts per grain changes the compression velocity throughout the formation in Walker Ridge 313H.

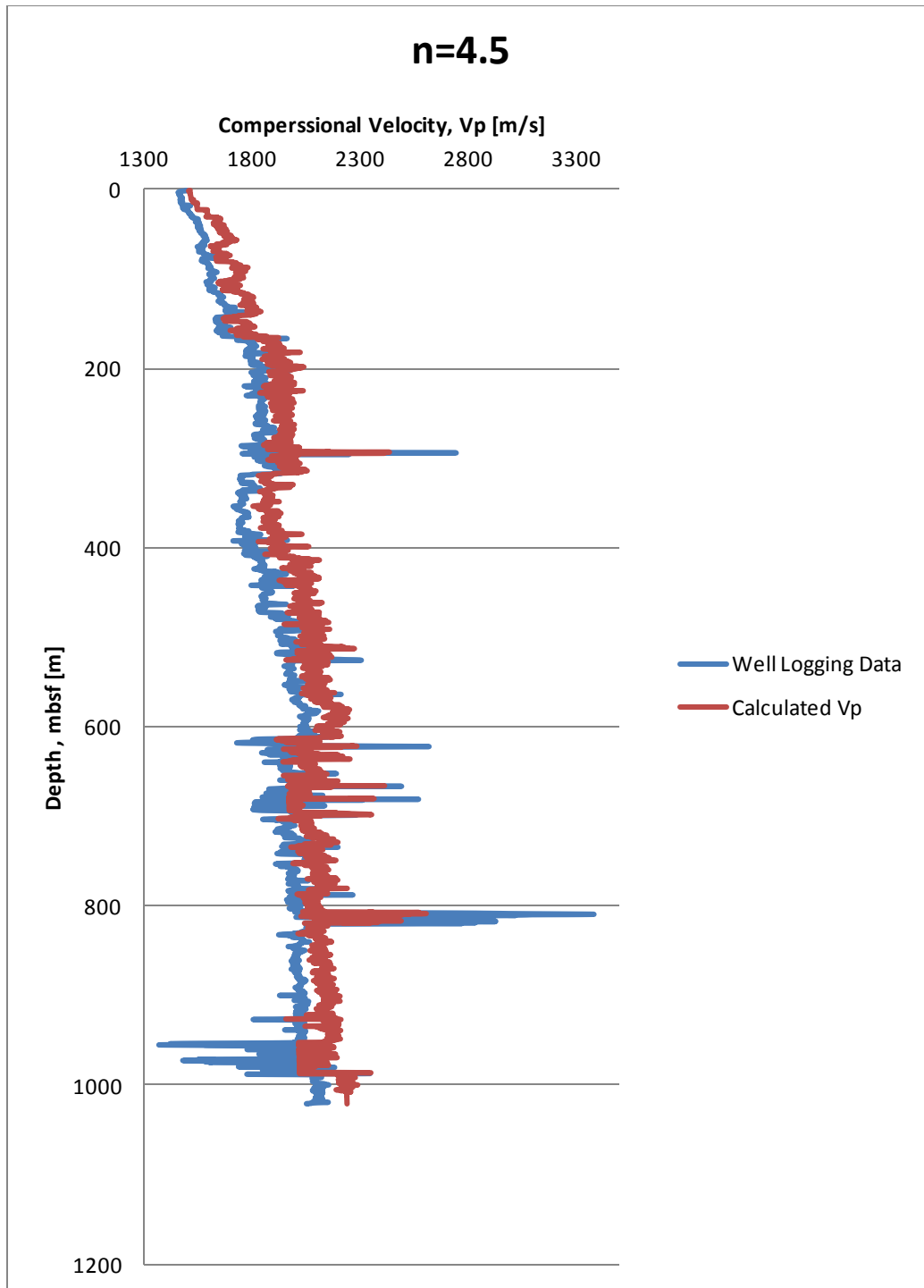


Figure 3.2: Orange line shows the compressional velocity for the model with an average of 4.5 contacts per grain. The model closely follows the same compressional velocity as the velocity from well-logging data from Walker Ridge 313H.

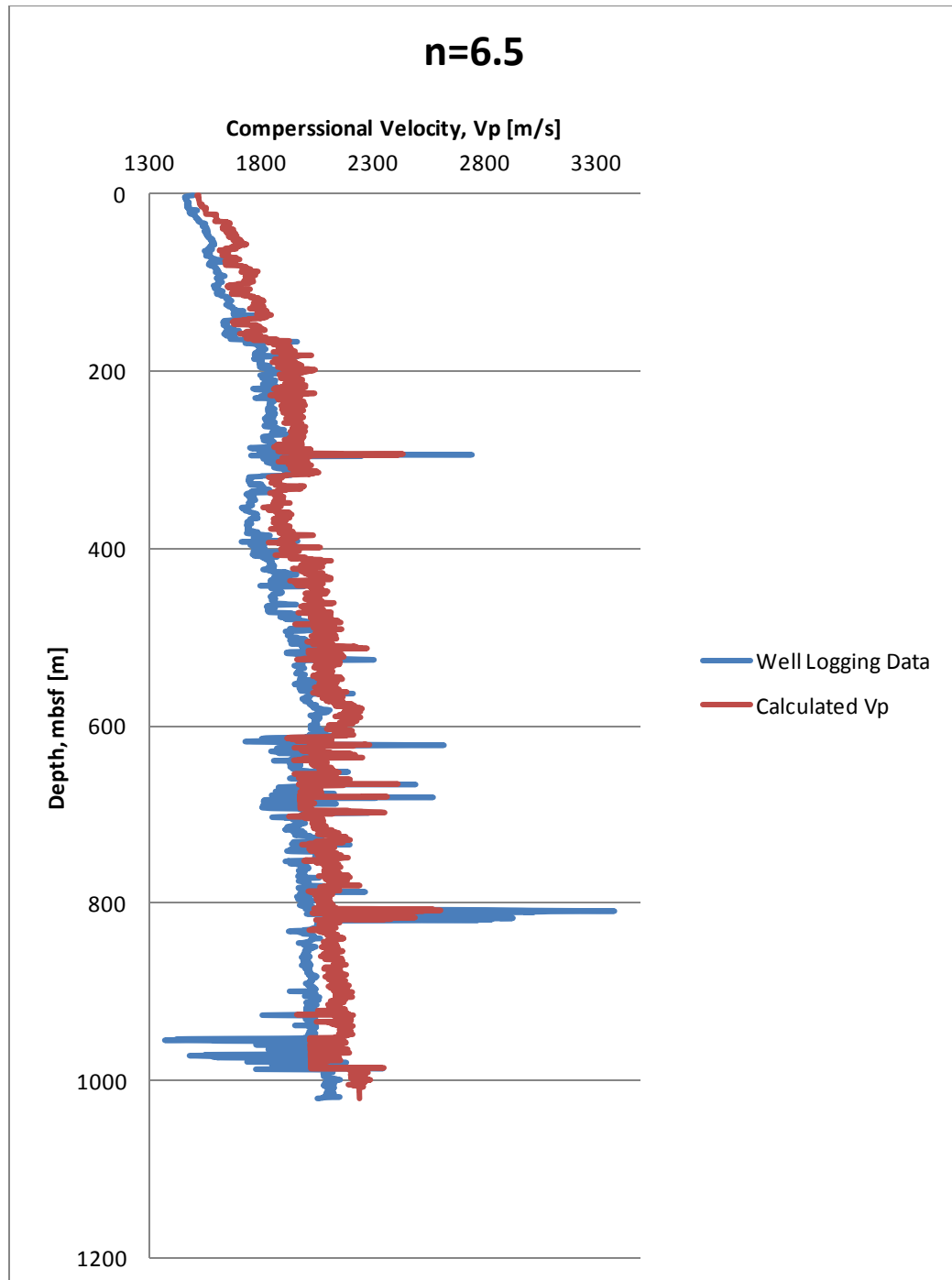


Figure 3.3: Illustrates the compressional velocity model at Walker Ridge 313H for an average of 6.5 contacts per grain. By comparing this result with Figure 3.2, it can be observed that the compressional velocities have increased and the line has shifted.

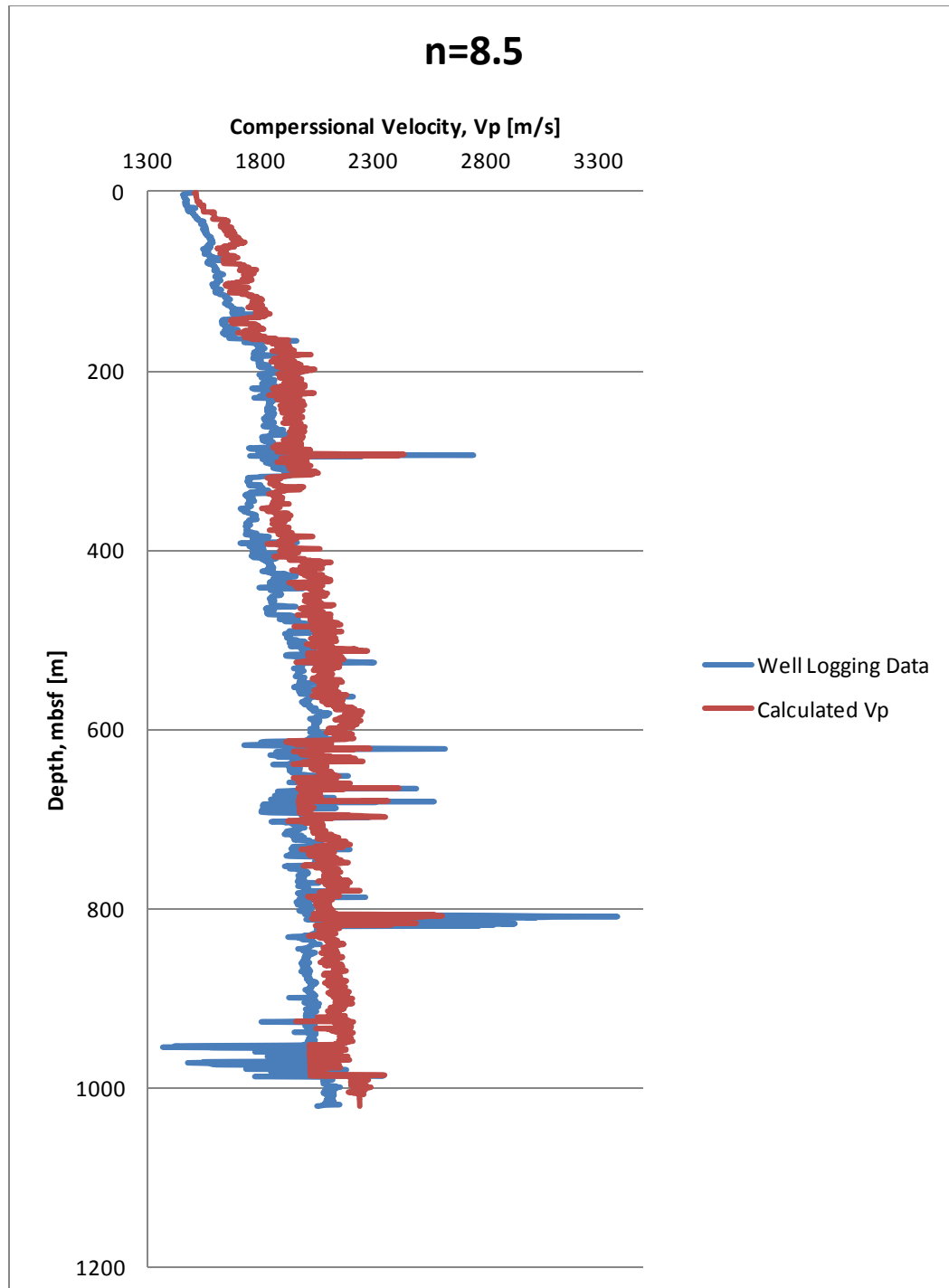


Figure 3.4: Illustrates the compressional velocity model at Walker Ridge 313H for an average of 8.5 contacts per grain. In this case, compressional velocities are greater than those in Figure 3.2 and 3.3.

These figures show that the model best follows the actual data from Walker Ridge well-logging data if 4.5 is chosen as the value for the average number of contacts per grain. This may suggest that the formation in the Walker Ridge site is relatively young and has not been compacted or consolidated by pressure and the environment. Minor changes in the average number of contacts per grain show how changes in lithology can greatly impact the compressional velocity. Figure 3.5 gives an overview of how a number of contacts per grain affects the compressional velocity.

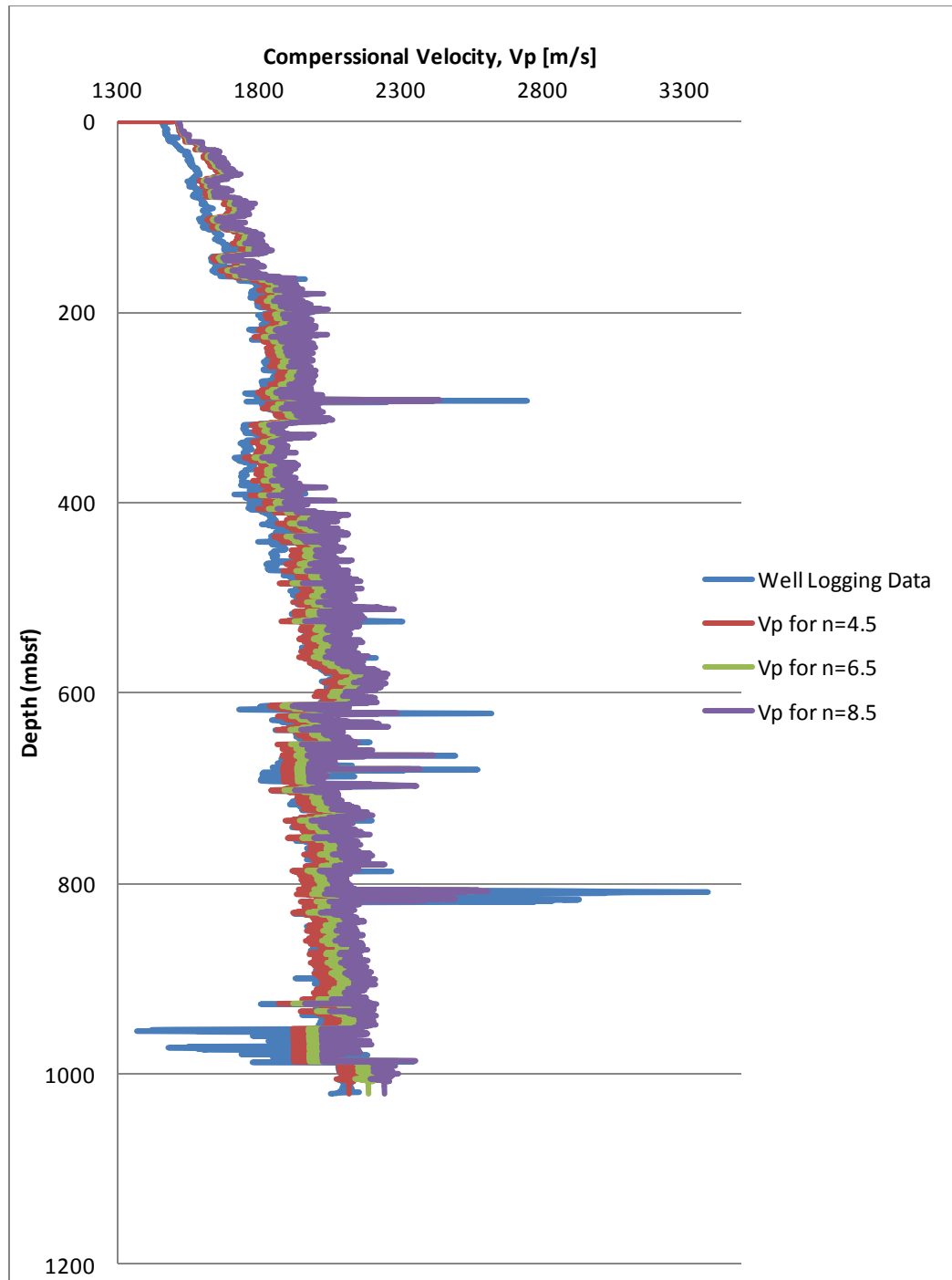


Figure 3.5: Illustrates the compressional velocity model at Walker Ridge 313H for an average of 8.5, 6.5, and 4.5 contacts per grain. As the number of contacts per grain decreases, calculated compressional velocity resembles more with the compressional velocity from well-logging data.

### **3.4: SYNTHETIC SEISMOGRAM**

#### **3.4.1: Overview**

This section presents how Interactive Petrophysics was used to create synthetic seismograms. To use this software, multiple variables must be determined. These variables include: acoustic velocities, travel time, and seismic wavelet data.

Acoustic velocities were determined using the equations provided in Chapter 2. A compressional velocity profile for a formation saturated with water was shown in the previous section. These velocities differ only in sections where different types of fluids and saturations are encountered.

The travel time can be found using two different methods. The first method is to find the travel time between each depth at which a velocity was calculated by calculating the change of depth divided by the velocity of that section. The second method is to use Interactive Petrophysics's "Create Time Curve" function. This function requires two variables of the sonic velocity which was obtained from well-logging data, and the true vertical depth. In this method, the travel time curve is created by integrating the data in sonic or velocity long over true vertical depth. For this study, the first approach was used and the one-way travel time of the wavelet then was determined to be 0.505 seconds through the formation.

### 3.4.2: Wavelet Preparation

The seismic wavelet used in this research is the actual wavelet that was generated and propagated into the formation. Figure 3.6 shows the generated wavelet used for seismic data acquisition at Walker Ridge.

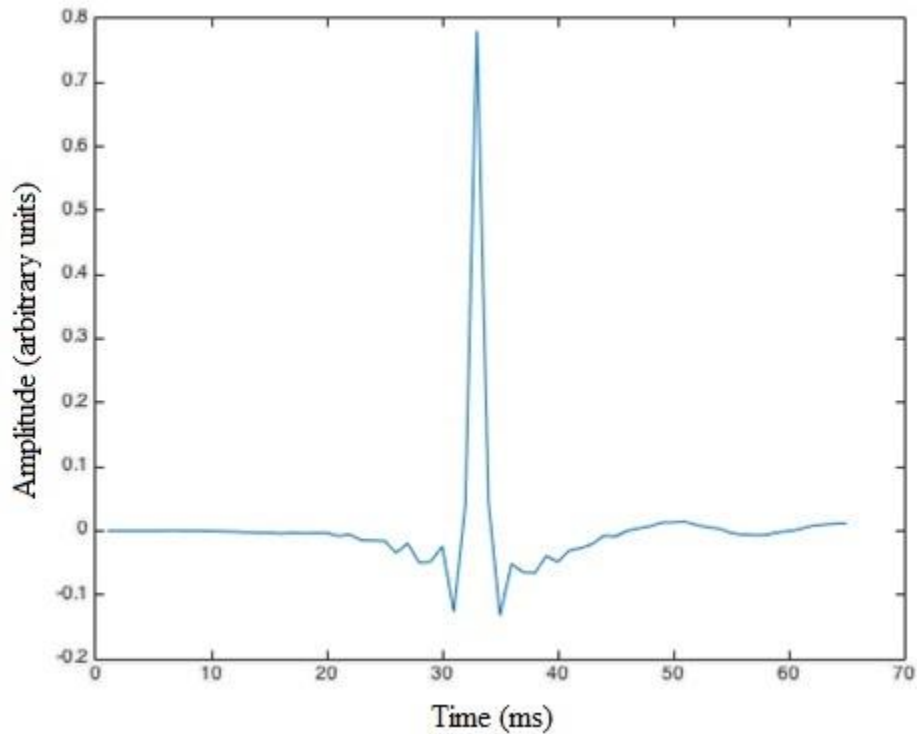


Figure 3.6: Shows the wavelet used for seismic acquisition at Walker Ridge (S. Haines, personal communication).

Figure 3.6 was then modified in order to satisfy Interactive Petrophysics requirements. After digitization, the data in X-axis was shifted such that the peak would be positioned at the time equal to zero. Figure 3.7 illustrates the modified seismic wavelet that was used in Interactive Petrophysics.

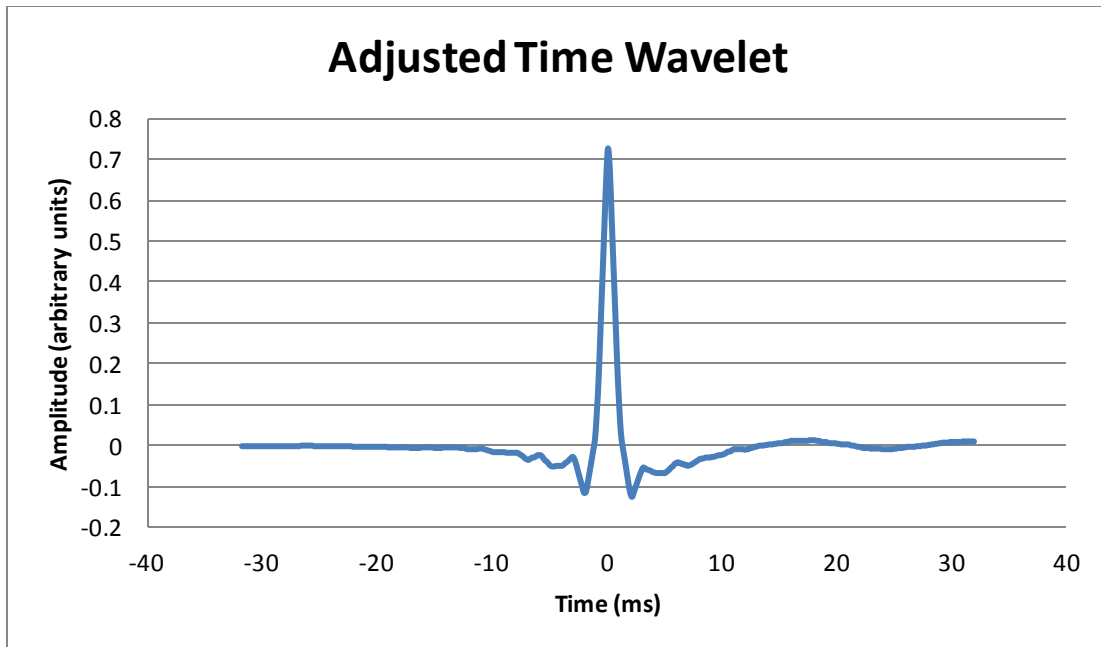


Figure 3.7: Shows modified seismic wavelet used in Walker Ridge for Interactive Petrophysics requirements.

### 3.4.3: Interactive Petrophysics

After adjusting the seismic wavelet along and determining the suitable number of contacts per grain, various models with different fluid saturations and three-phase zone thicknesses were to be created. Unlike many programs, models created in Interactive Petrophysics must be created individually.

In order to find the acoustic velocities in IP, codes of formulas must be written for the following variables, and then to be calculated in order presented: density of pore fluid ( $\rho_f$ ), bulk density of solid ( $\rho_s$ ), Poisson's ratio ( $\nu$ ), effective pressure (P), Hertz-Mindlin elastic moduli ( $K_{HM}, G_{HM}$ ), Hashin-Strikam dry bulk and shear moduli ( $K_{dry}, G_{dry}$ ), and saturated bulk and shear moduli ( $K_{sat}, G_{sat}$ ). Using equations (2.3) and (2.4) presented in Chapter 2 will allow us to find the acoustic velocities ( $V_p, V_s$ ).

Variables travel time, acoustic velocities, and adjusted seismic wavelet can now be used in IP's advanced interpretation tooltip to create synthetic seismograms. This procedure must be followed for each model created. Furthermore, IP uses Aki and Richards (1980) approximation of the Zoeppritz equations where solution sought for has zero-offset intercept and slope.

## **Chapter 4: Data and Results**

### **4.1: OVERVIEW**

This chapter presents the results produced in this study, compares created models, and presents the amplitude versus angle of incidence results in tabular format. The results show the effect of fluid saturation and thickness variation on the creation of the synthetic seismograms.

### **4.2: VELOCITY PROFILES**

#### **4.2.1: Fluid Saturation**

Fluid saturation plays an important role in the creation of the synthetic seismograms. For example, a small variation in gas saturation has a large impact on the creation of synthetic seismograms, while the variation in hydrate and water saturations may not contribute as much to the creation of synthetic seismograms.

In this section, models with different fluid saturations are presented. This includes the variation of hydrate and gas saturation between 1% to 5% and zero to 50% respectively for a three-phase zone with 5 meter thickness. The hydrate stability zone is located at 882 meters below the seafloor in sandy layers and at 885 mbsf in clay layers (Bihani, 2016). For ease of work depth of 880 mbsf was used as the base for fluid substitution.

Note: In all figures presented in this paper, the annotation (e.g. 69-01-30-5) indicated the saturation and thickness of the 3-phase zone. These annotations refer to water saturation, hydrate saturation, gas saturation, and thickness respectively. For example, annotations 69-01-30-5, indicates water saturation of 69%, hydrate saturation of 1%, free gas saturation of 30%, and 3-phase zone thickness of 5 meters.

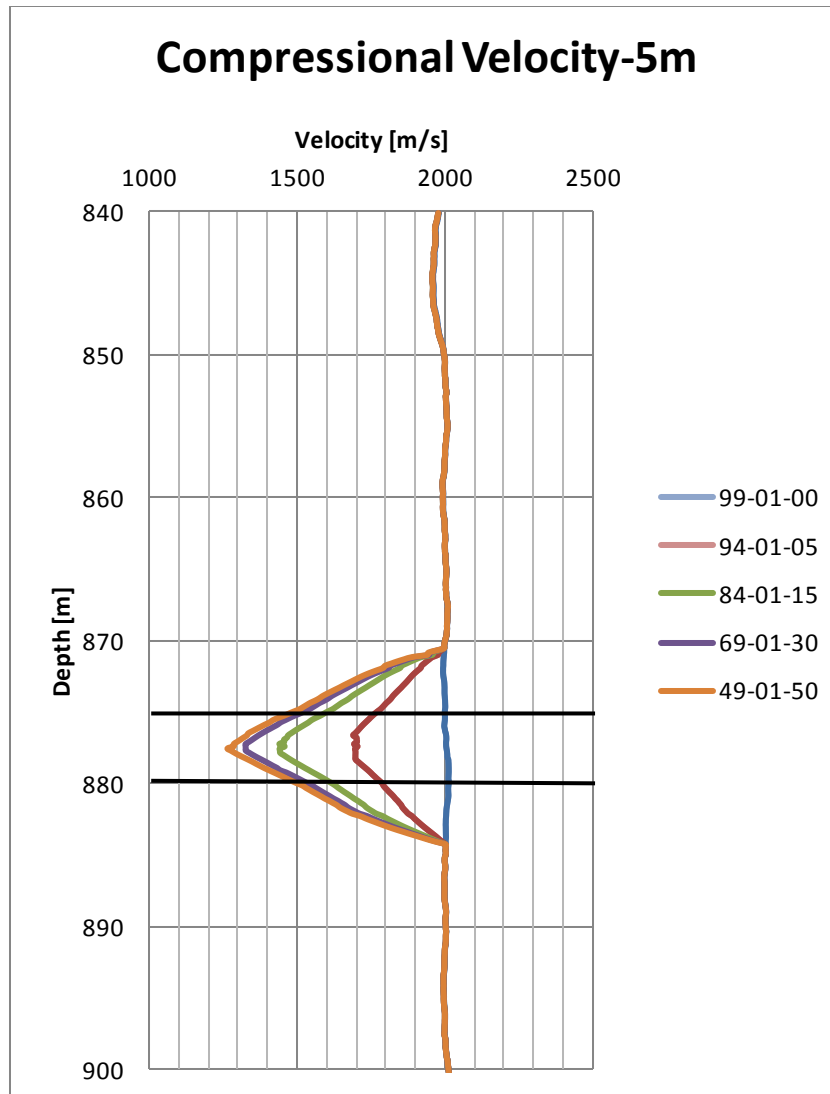


Figure 4.1: This figure presents the compressional velocity versus depth where hydrate saturation is 1% in the 3-phase zone and gas saturation is increasing for each case (increasing gas saturation in 5 meters 3-phase zone) The compressional velocity does not change for the case where 1% hydrates are encountered. This is reasonable as hydrate do not change the elastic properties. As expected, when the gas saturation is increased, the compressional velocity decreases by 300 m/s for the first 5% gas substitution instead of water. As the gas content increases however, the increment of velocity drop, decreases to 250 m/s for 10% gas substitution. This decrease continues and reaches its minima 1200 m/s for 50% gas substitution.

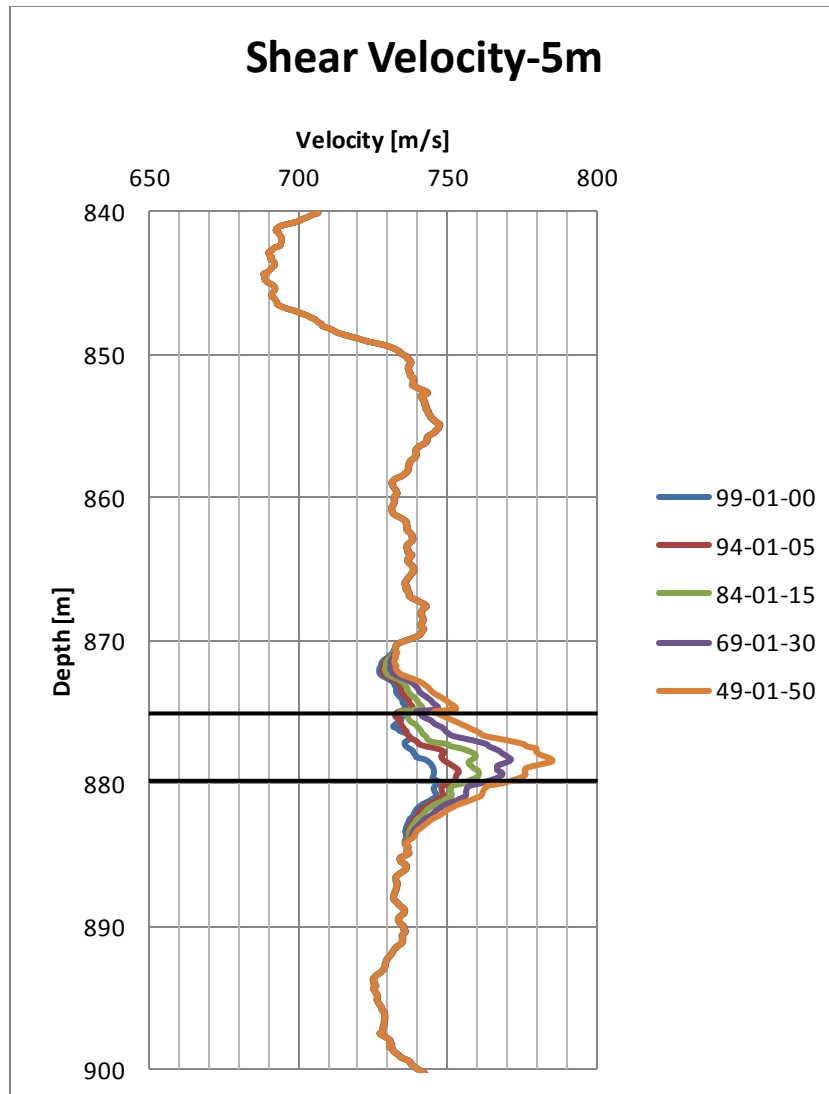


Figure 4.2: This figure presents the shear velocity versus depth for the same case as Figure 4.1, where 3-phase zone contains 1% hydrate saturation with increasing gas saturation. Results show that as the gas saturation increases, the shear velocity increases by a small amount. The shear velocity increases by about 10 m/s for each presented model as gas saturation increases.

Same observations and conclusions were found for different cases with different hydrate saturation of 3% and 5%. Figures 4.3 and 4.4, presented below shows the results for these cases.

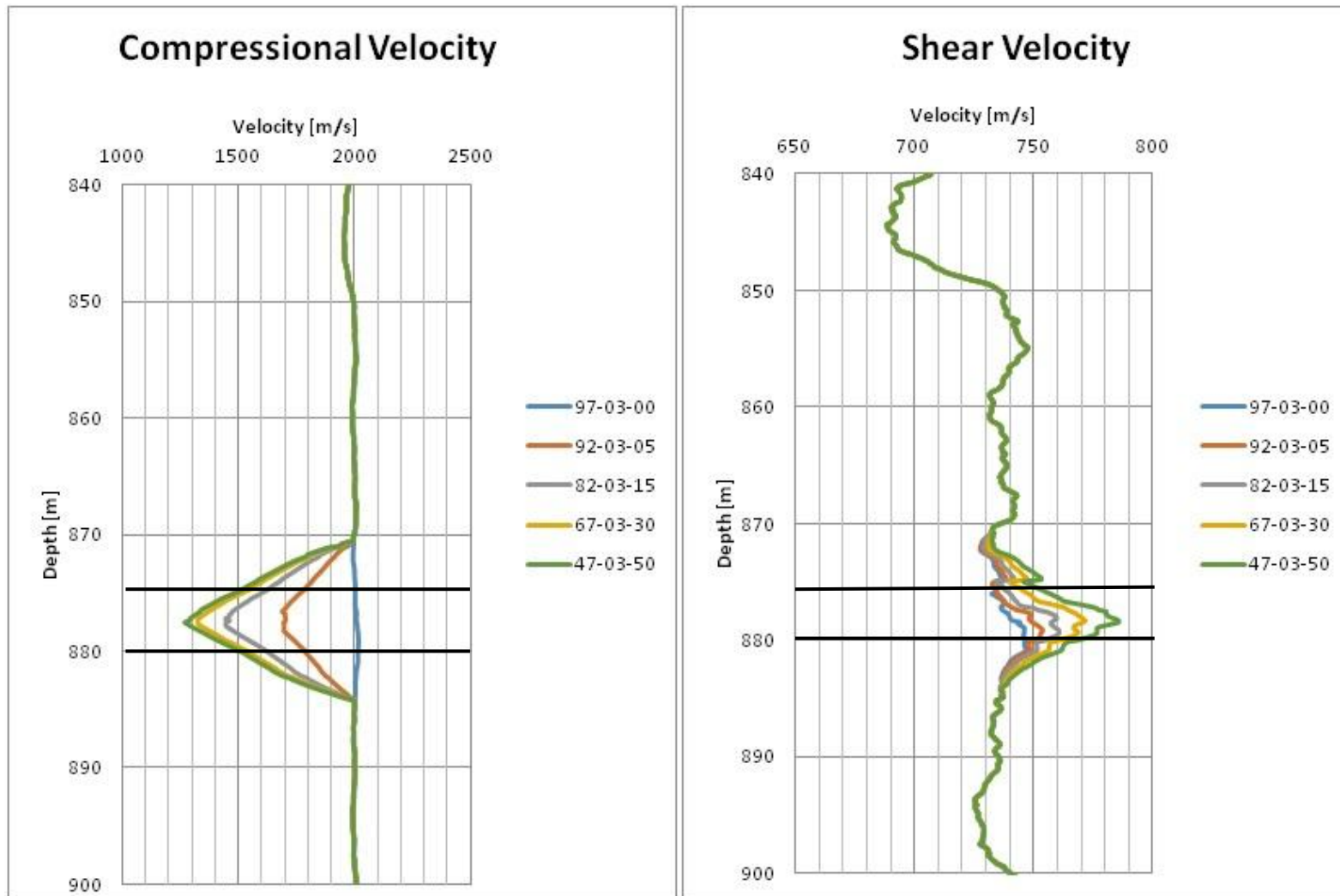


Figure 4.3: This figure presents the compressional velocity (on left) and shear velocity (on right) versus depth for a case where the hydrate saturation is 3% in 5 meters 3-phase zone with increasing free gas saturation. Results and conclusions are as same as the case with 1% hydrate saturation (Figures 4.1 and 4.2).

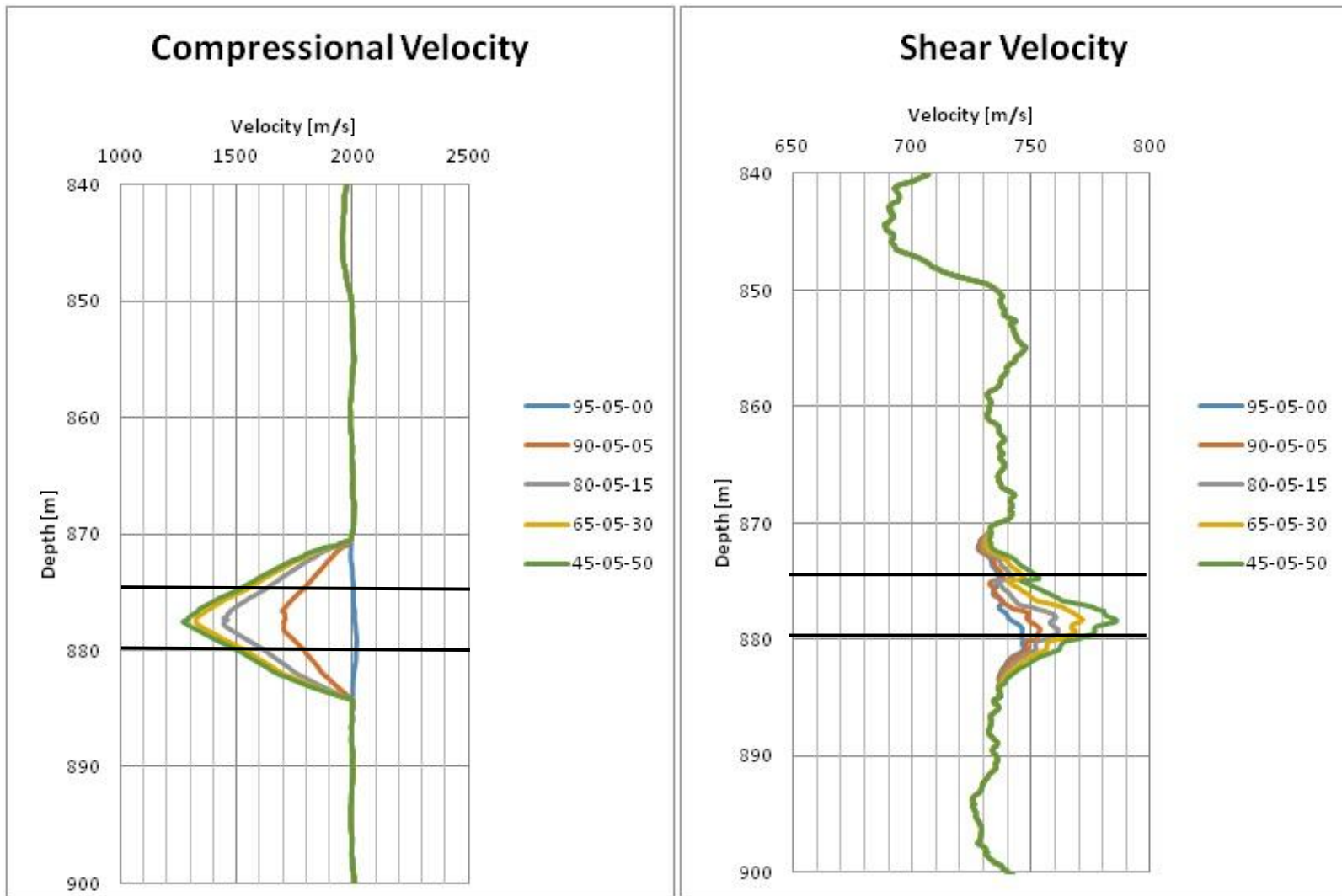


Figure 4.4: This figure presents the compressional velocity (on left) and shear velocity (on right) versus depth for a case where the hydrate saturation is 5% in 5 meters 3-phase zone with increasing free gas saturation.

#### 4.2.2: Fluid Saturation Comparison

Figure 4.5 compares the compressional velocity for multiple cases of same gas saturation versus different hydrate saturation. For the case of 5% gas saturation (Figure 4.5c), we can observe that for higher hydrate saturation, the compressional velocity is slightly higher. Figure 4.5a presents the models with 50% gas saturation. It may not be visible, but for the case with higher hydrate saturation, the compressional velocity is higher by 0.4 m/s for extra 2% hydrates. Results show that for high gas saturation, low abundance of hydrate does not affect the compressional velocity as the velocities are almost identical. In addition, since the layer is thin, the velocity signature does not reach to a constant value compared to the case of 5% gas saturation.

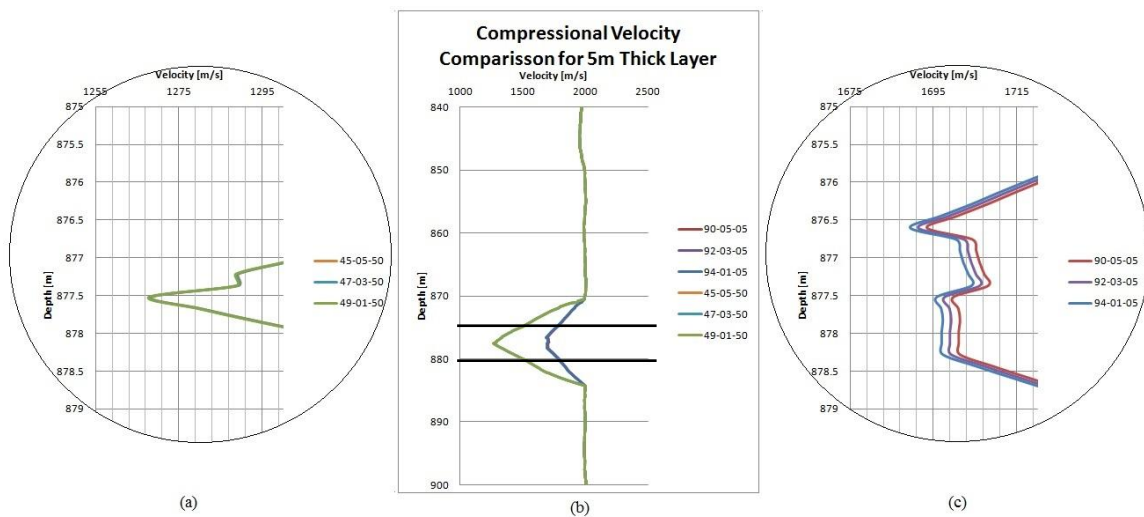


Figure 4.5: In high free gas saturation (on left) the hydrate saturation does not affect the compressional velocity. However, in low free gas saturation of 5%, small change of hydrate saturation is a factor in compressional velocity.

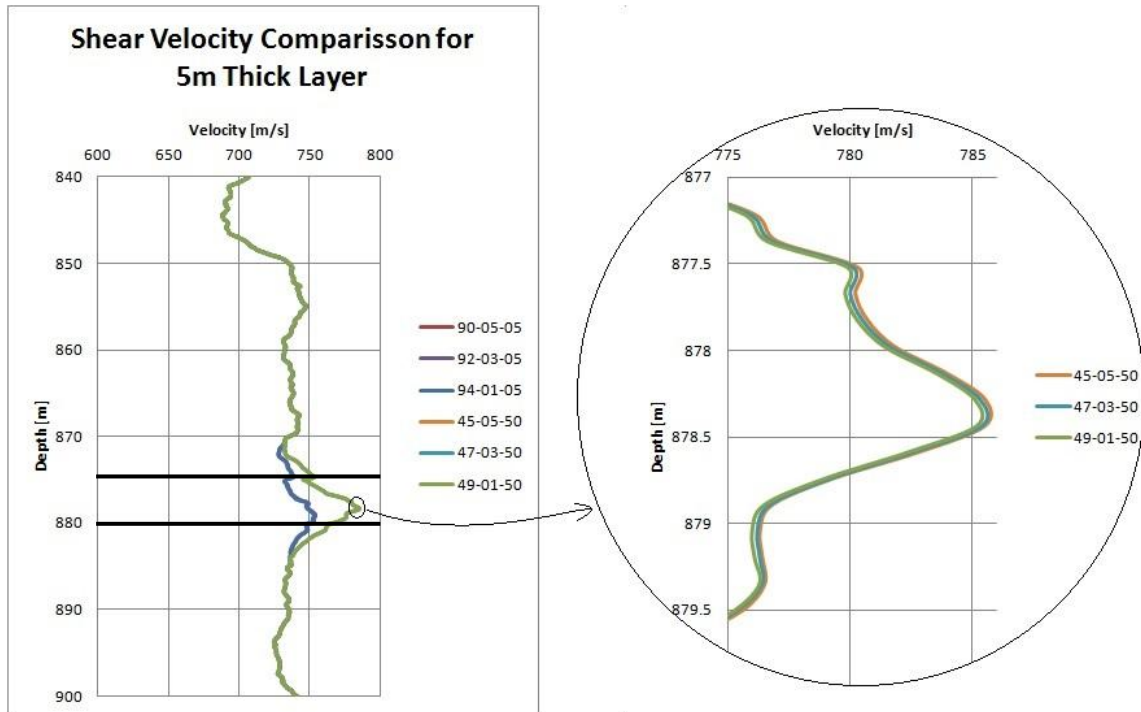


Figure 4.6: Comparison of shear velocity for sets two sets of models of 5% and 50% gas saturation with different hydrate saturation. The velocity difference between cases with 1%, 3%, and 5% hydrate saturation is so minimal that it is not observable. For each 2% increment increase of hydrate saturation, the shear velocity increases by 0.1 m/s. The same scenario applies to the sets of models with 50% gas saturation.

### **4.2.3: 3-Phase Zone Thickness Variation**

In this section, models with different 3-phase zone thickness are presented. This includes 3-phase zone thicknesses of 10 m and 30 m (5 m 3-phase zone was presented in the previous section). The thickness of the 3-phase zone affects the seismic response and determines how easily detectable the 3-phase zone is. Figures 4.7 and 4.8 show the results for 3-phase zone thickness of 10 meters.

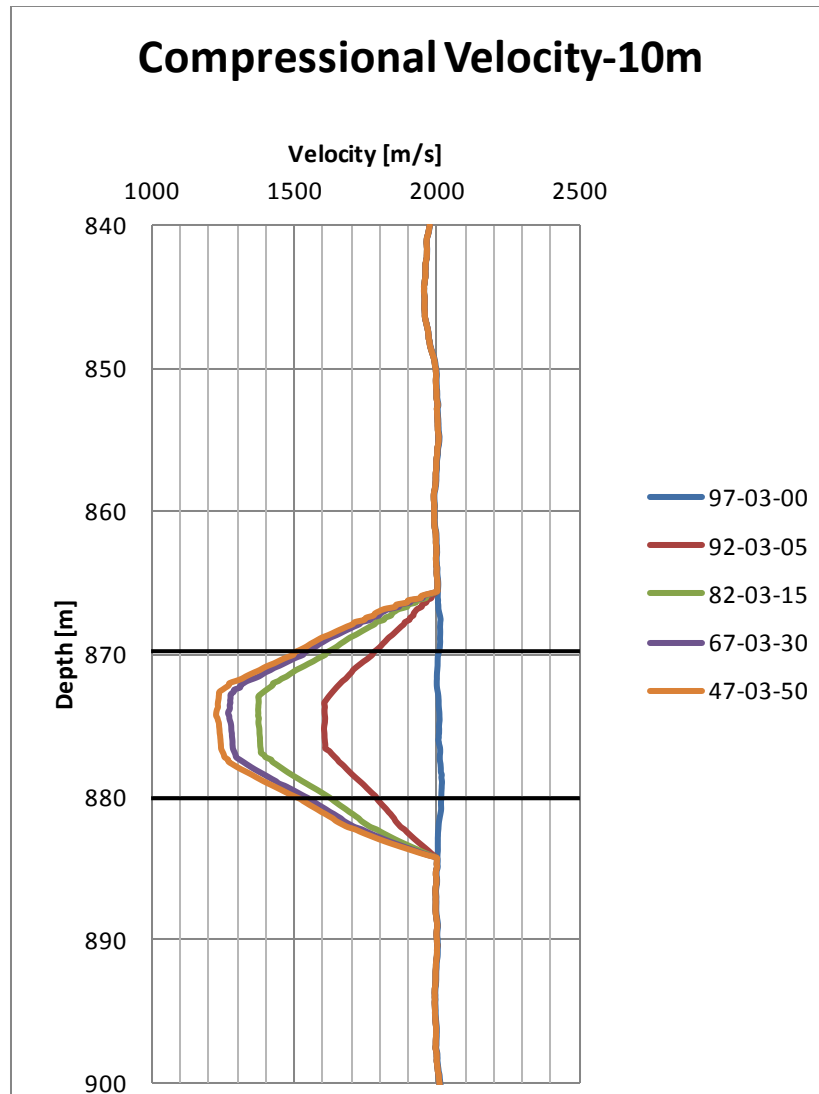


Figure 4.7: This figure presents the compressional velocity versus depth for a 3-phase zone with 3% hydrate saturation. The thickness is enough for the compressional velocity to reach its minimum. For example, for the case of “92-03-05”, the compressional velocity drops to 1600 m/s for 4 meters continuously. Furthermore, like the model presented in the previous section, as the gas saturation increases, the compressional velocity decreases.

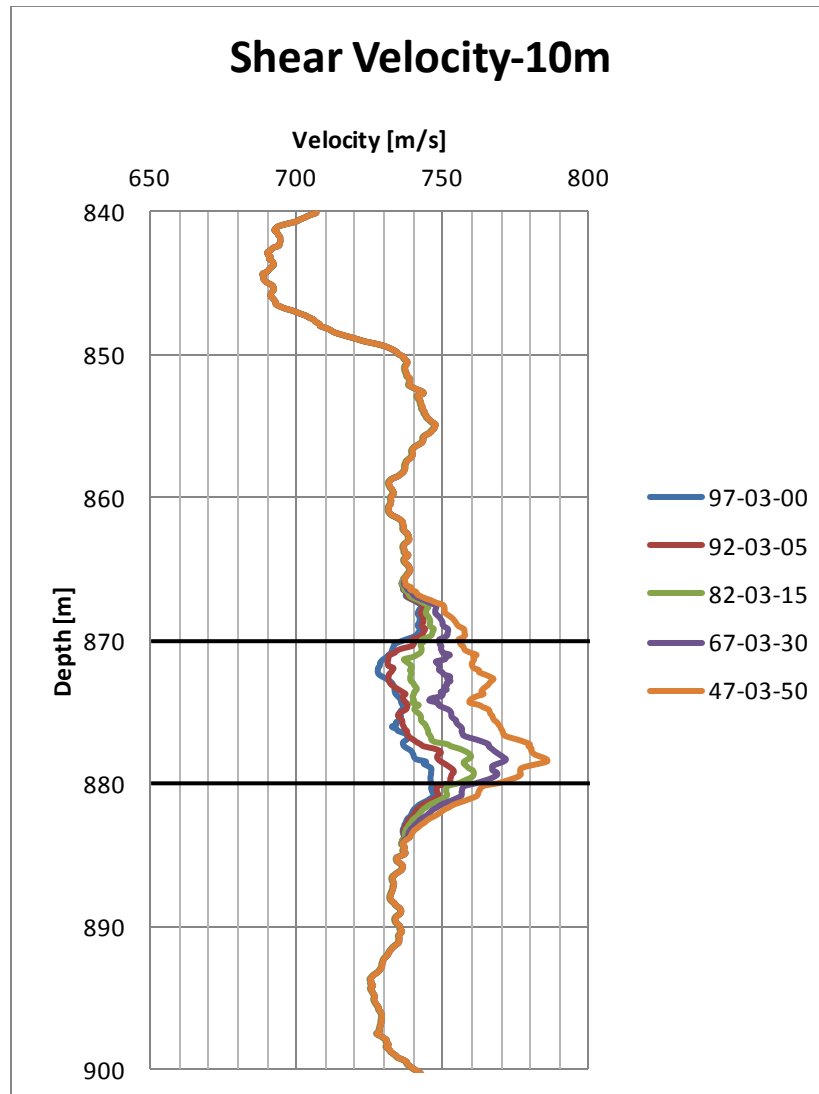


Figure 4.8: This figure presents the shear velocity versus depth for the same cases as Figure 4.7, where 3-phase zone contains 3% hydrate saturation with increasing gas saturation. Like the results shown in the previous section, as the gas saturation increases, the shear velocity increases by a small amount. The shear velocity increases by about 10 m/s for each presented model for each increment increase of gas saturation.

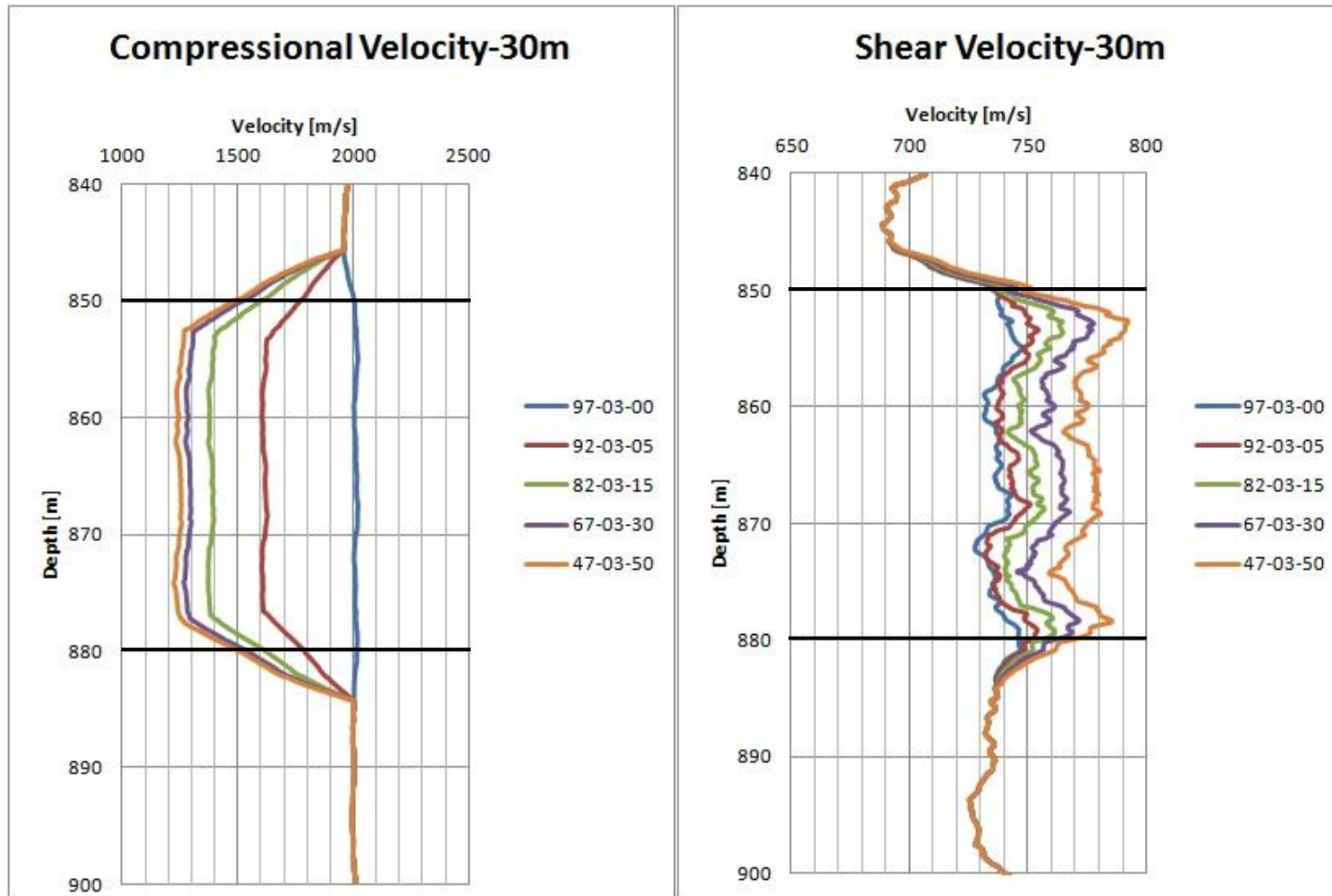


Figure 4.9: This figure presents the compressional velocity (on left) and shear velocity (on right) versus depth for a case where the hydrate saturation is 3% in a 30 m 3-phase zone with increasing free gas saturation.

#### **4.2.4: 3-Phase Zone Thickness Variation Comparison**

In this section, acoustic velocities for models with 3% hydrate saturation and different 3-phase zone thicknesses (5, 10, and 30 m) are compared. Figure 4.10 illustrates how the compressional velocity for the models with 10 and 30 m 3-phase zones reaches its minimum and stays at the same value throughout the layer. For the case of a 5 m 3-phase zone, it is observable that the compressional velocity does not reach its minimum. It can be concluded that the thinner the layer is, the harder compressional velocity's signature is to observe. Furthermore, this will affect the visibility of BSR in synthetic seismograms.

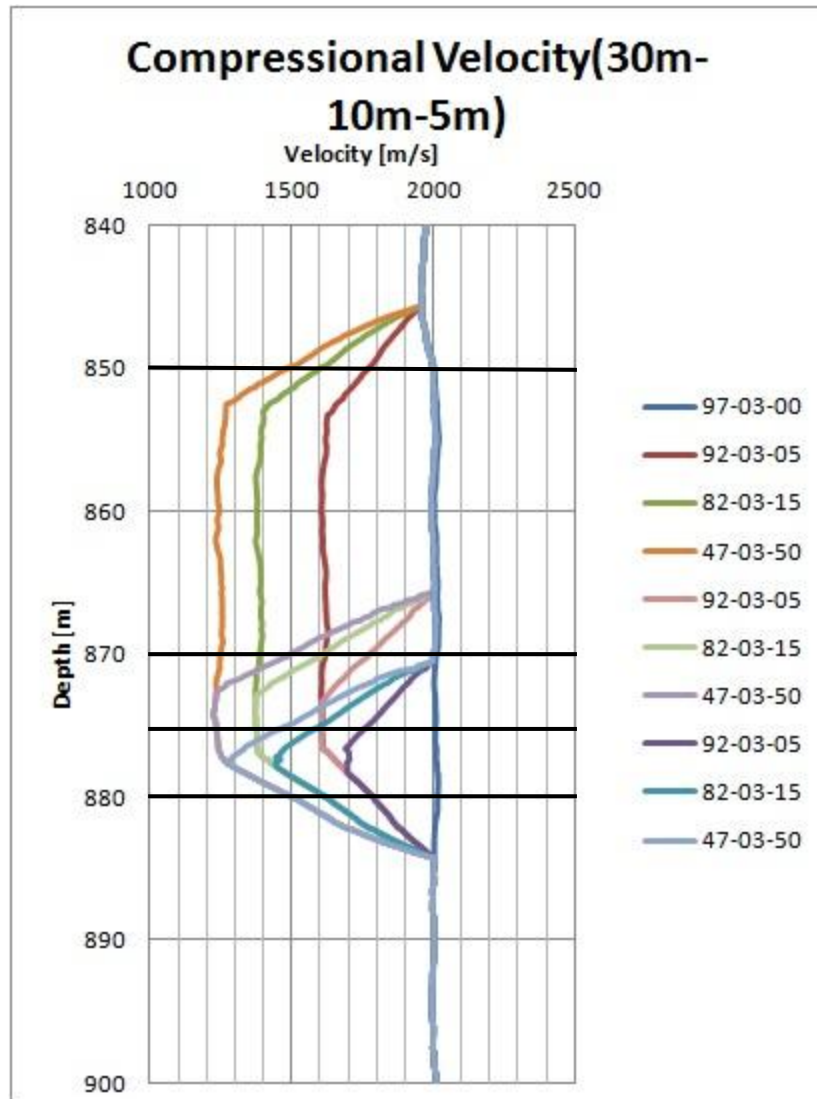


Figure 4.10: This figure presents the compressional velocity versus depth for all models containing 3% hydrate saturation with multiple free gas saturations and 3-phase zone thicknesses.

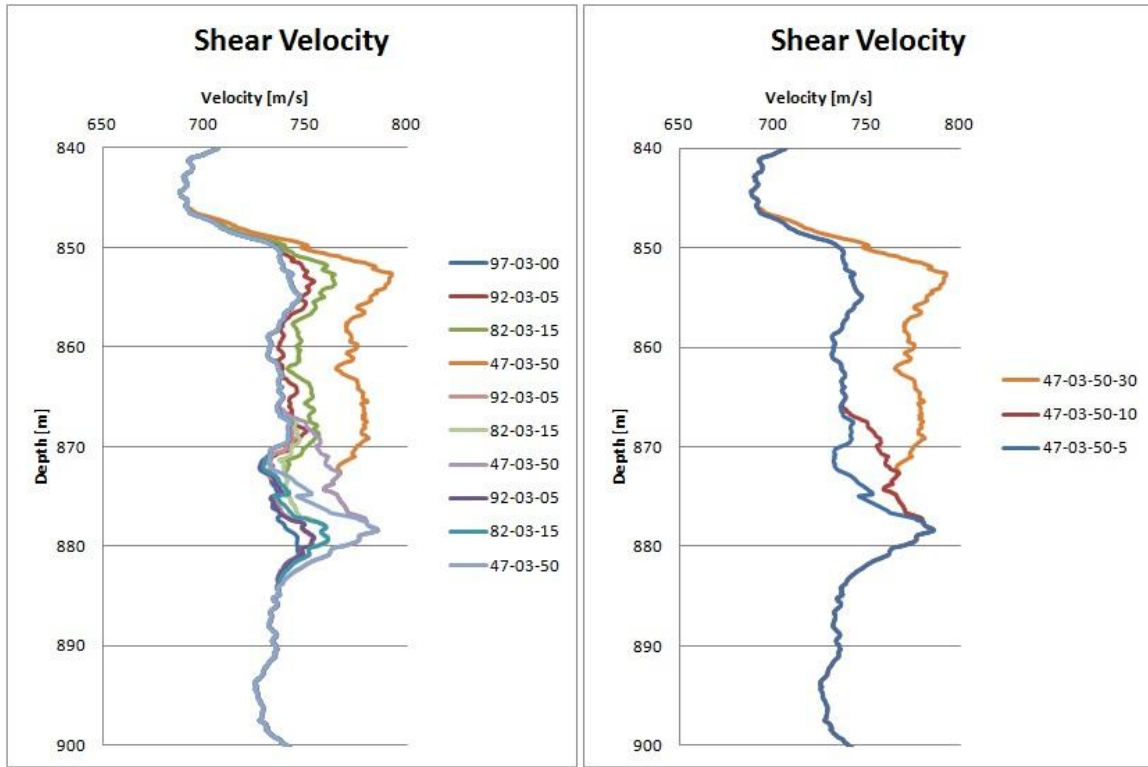


Figure 4.11: Figure 4.11a shows the shear velocities for the same models in Figure 4.10. Since it is hard to follow and distinguish between each case, Figure 4.11b is presented. Figure 4.11b presents the same saturation models with different thickness zones of 5, 10, and 30 meters.

### 4.3: SYNTHETIC SEISMOGRAM

#### 4.3.1: Fluid Saturation

Fluid saturation plays an important role in the creation of the synthetic seismograms. For example, a small variation in gas saturation has a large impact on the character of synthetic seismogram, while the variation in hydrate and water saturations may not contribute as much to the character of the synthetic seismogram.

Figure 4.12 illustrates the seismic profile of WR's 313H, assuming that the porous media is saturated with water.

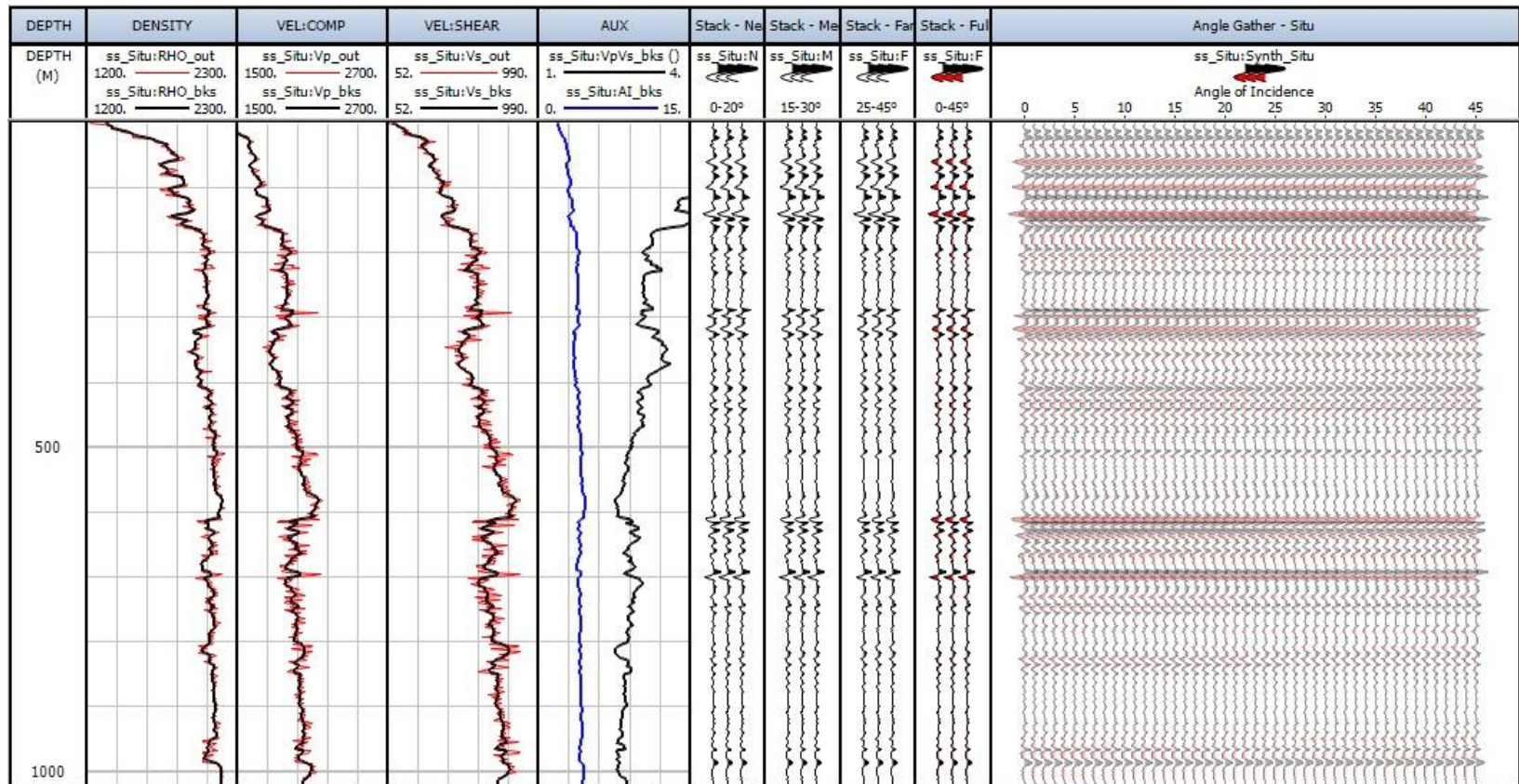


Figure 4.12: Illustrates the seismic profile for Walker Ridge 313H where the porous media is saturated with water. Seismic reflections in this case are due to changes in porosity rather than fluid type.

Fluids to be substituted for water are hydrate and free gas. For the first set of the synthetic seismogram models, the 3-phase equilibrium zone was set to be 5 meters thick with a constant hydrate saturation of 3% while free gas was increased and substituted instead of water. All of the presented figures will show depths 800 to 1000 meters.

***Water-Hydrate-Free Gas Saturation (97-03-00-5m):***

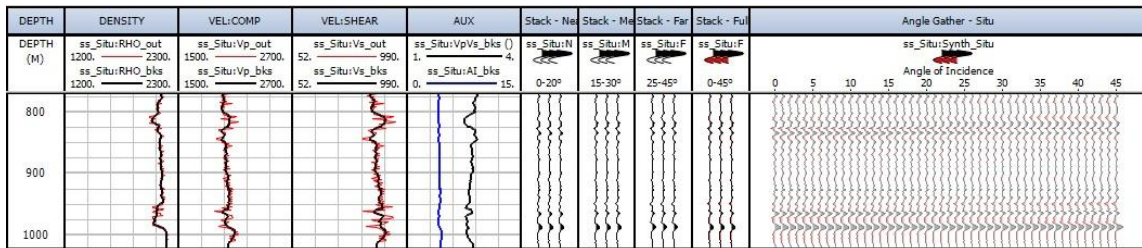


Figure 4.13: Synthetic seismograms for a 2-phase equilibrium zone containing 3% hydrate and zero free gas. The result looks similar to Figure 4.12 where layers are 100% saturated with water. Hydrates do no contribute in creation of BSR at low saturations.

***Water-Hydrate-Free Gas Saturation (92-03-05-5m):***

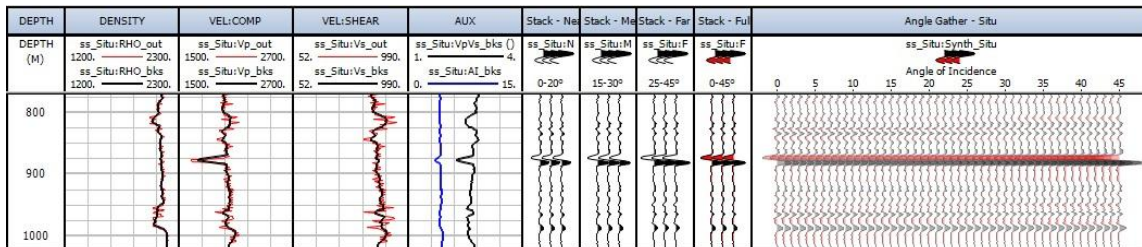


Figure 4.14: Seismic signature for a 3-phase equilibrium zone containing 3% hydrate and 5% free gas. As the free gas is substituted instead of water by 5% compared to the previous case (Figure 4.13), a profound seismic signature of BSR becomes observable around 880 mbsf. Compressional velocity greatly reduces as free gas is introduced in the model, which results in a strong negative reflection.

**Water-Hydrate-Free Gas Saturation (82-03-15-5m):**

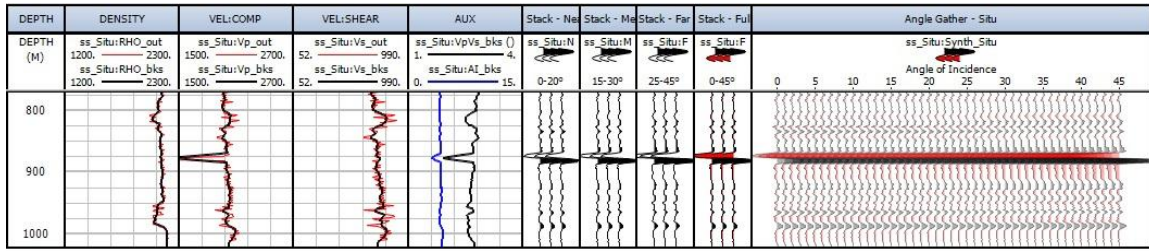


Figure 4.15: Seismic signature for a 3-phase equilibrium zone containing 3% hydrate and 15% free gas. Compared to Figure 4.14, extra 10% free gas makes this seismic signature sharper and more profound.

**Water-Hydrate-Free Gas Saturation (67-03-30-5m):**

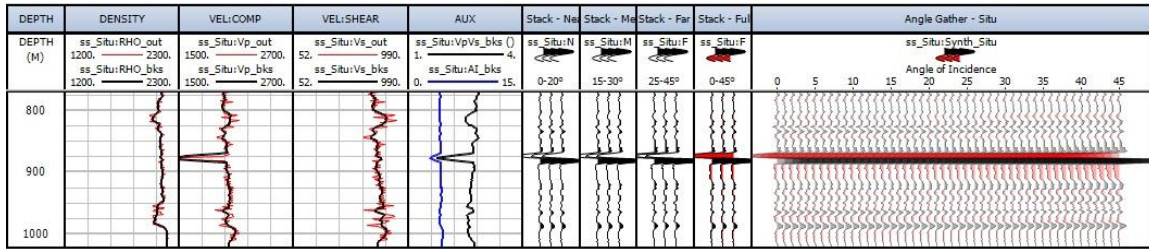


Figure 4.16: Seismic signature for a 3-phase equilibrium zone containing 3% hydrate and 30% free gas. Due to the larger drop of compressional velocity, results show sharper peaks and troughs. As shown in compressional compression velocity curves, velocities for cases with high free gas saturation reach minima, which results in similar looking seismic signatures (BSRs).

**Water-Hydrate-Free Gas Saturation (47-03-50-5m):**

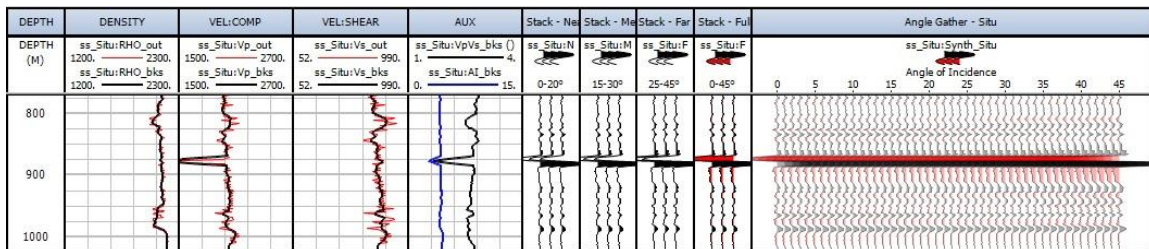


Figure 4.17: Seismic signature for a 3-phase equilibrium zone containing 3% hydrate and 50% free gas.

As mentioned before, low hydrate saturations do not contribute or change results in the creation of the BSR. Compressional velocity changes by ~5 m/s for each 2% of hydrate added or deducted; as a result, models with hydrate saturation of 1% and 5% look similar to the ones shown above (Figures 4.13-4.17). Results for these models are not presented in this thesis as they look identical to these models.

### 4.3.2: Thickness

In this section, synthetic seismogram models with different 3-phase zone with the thickness of 10 and 30 m are presented (a 5 m 3-phase zone was presented in the previous section). As shown in the previous section, while fluid saturation has a direct connection with acoustic velocities and synthetic seismograms, the thickness of the 3-phase zone would make these properties to be more easily visible in seismic data. Figures below (4.18 to 4.22) present the synthetic seismograms for 10 m thick 3-phase equilibrium zone.

#### *Water-Hydrate-Free Gas Saturation (97-03-00-10m):*

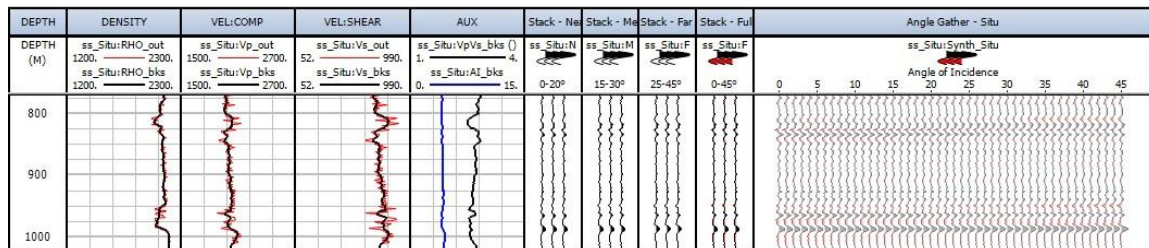


Figure 4.18: Synthetic seismograms for a 10 m 3-phase equilibrium zone containing 3% hydrate and 0% free gas. Due to low hydrate saturation, no seismic reflections are seen. Results of this figure look identical to 5 m thickness model, Figure 4.13.

**Water-Hydrate-Free Gas Saturation (92-03-05-10m):**

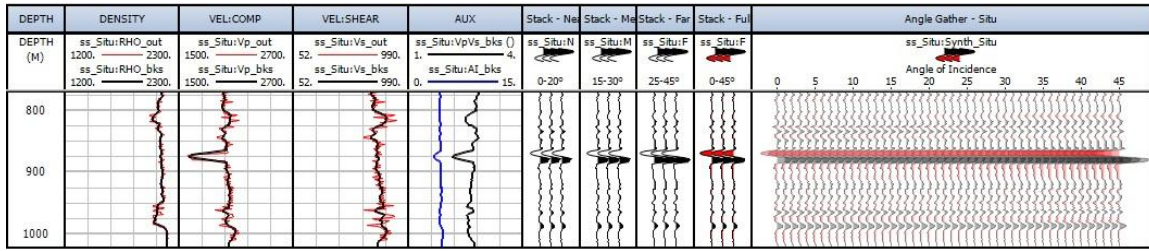


Figure 4.19: Seismic signature for a 10 m 3-phase equilibrium zone containing 3% hydrate and 5% free gas. Comparing this model with the 5 m model, Figure 4.14, it is observable that the peak and trough of the seismic reflections are not squeezed against one another.

**Water-Hydrate-Free Gas Saturation (82-03-15-10m):**

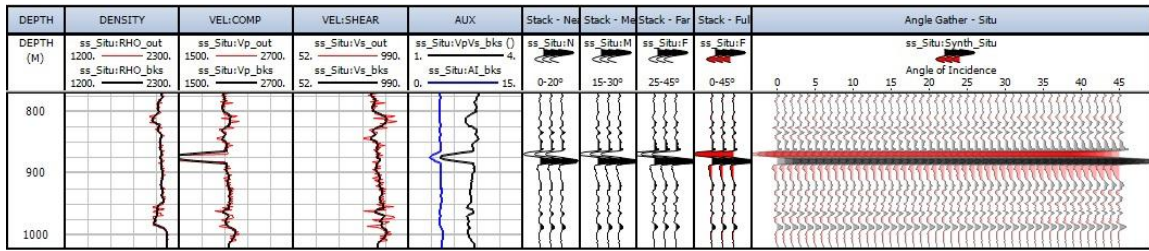


Figure 4.20: Seismic signature for a 10 m 3-phase equilibrium zone containing 3% hydrate and 15% free gas. Compared to Figure 4.19, extra 10% free gas makes this seismic reflection sharper and more profound.

**Water-Hydrate-Free Gas Saturation (67-03-30-10m):**

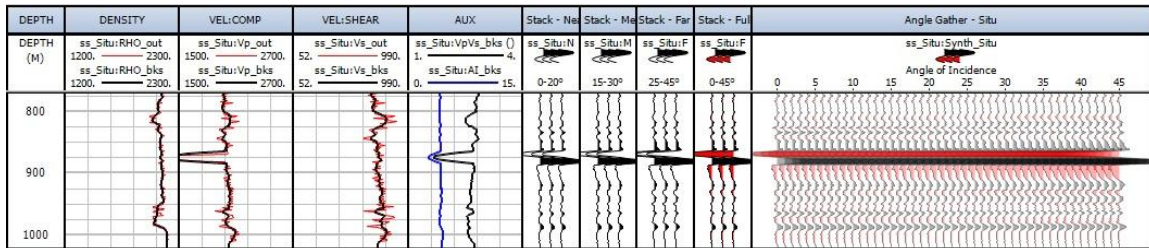


Figure 4.21: Seismic signature for a 10 m 3-phase equilibrium zone containing 3% hydrate and 30% free gas.

**Water-Hydrate-Free Gas Saturation (47-03-50-10m):**

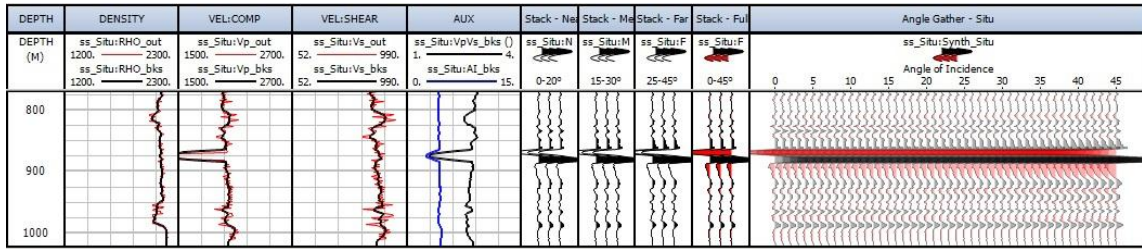


Figure 4.22: Seismic signature for a 10 m 3-phase equilibrium zone containing 3% hydrate and 50% free gas.

As shown previously in this section, most of the models look similar. Therefore, models with zero and 30% free gas saturations are skipped. Figures 4.23 to 4.25 present the models for the rest of the tested free gas saturations.

**Water-Hydrate-Free Gas Saturation (92-03-05-30m):**

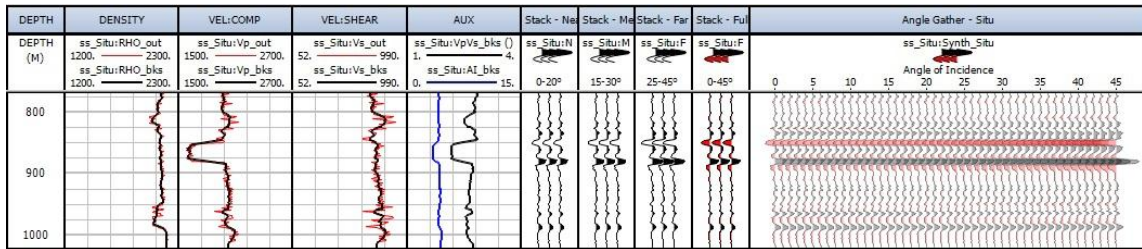


Figure 4.23: Seismic signature for a 3-phase equilibrium zone containing 3% hydrate and 5% free gas. Comparing this model with the 5 and 10 m models (Figure 4.14 and 4.19), the trough is not as strong in amplitude. In addition, the peaks of this seismic wavelet on both side of the trough are clear and distinguishable.

**Water-Hydrate-Free Gas Saturation (82-03-15-30m):**

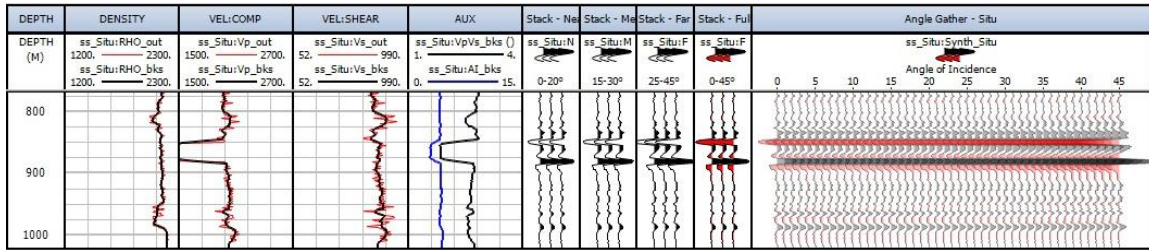


Figure 4.24: Seismic signature for a 3-phase equilibrium zone containing 3% hydrate and 15% free gas. Compared to Figure 4.23, the extra 10% free gas makes this seismic reflection stronger.

**Water-Hydrate-Free Gas Saturation (47-03-50-30m):**

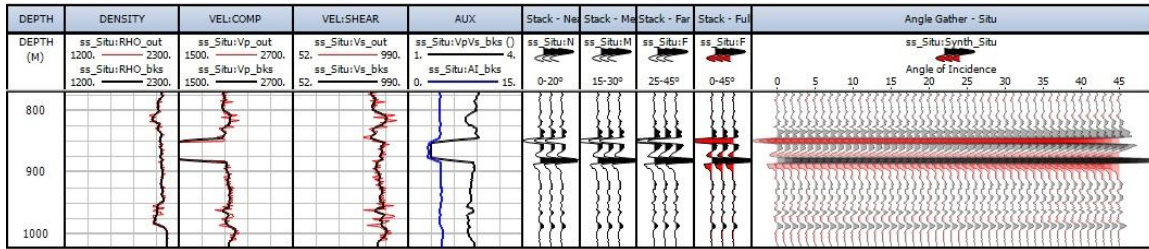


Figure 4.25: Seismic signature for a 3-phase equilibrium zone containing 3% hydrate and 50% free gas. The main trough of this model is what to be looked for when looking for the BSR.

**4.4: SPECIAL CASES**

Further work was done in order to better understand the effect of different fluid saturations on acoustic velocities and synthetic seismograms. This includes better a understanding of hydrates and the transition between layers with different saturations.

**4.4.1: Pure Hydrate**

This section presents the produced results for the cases with high hydrate saturations of 10, 30, and 50% percent (no free gas is in pores).

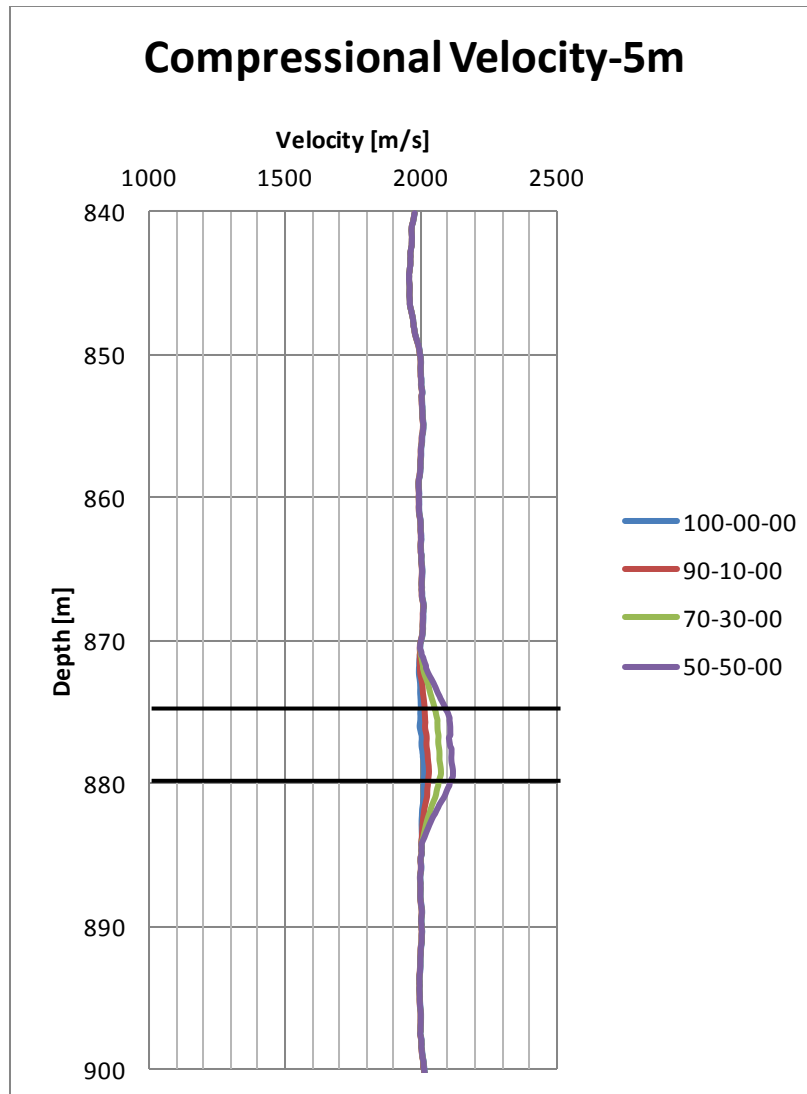


Figure 4.26: This figure presents the compressional velocity versus depth for the cases with 10, 30 and 50% hydrate saturation and with a thickness of 5 m. As previously concluded, the compressional velocity does not increase with low hydrate saturations. The increase of hydrate saturation begins to be noticeable in layers with more than 10% hydrate saturation. Compressional velocity increases by ~20 m/s for each 10% increase of hydrate saturation. Unlike the case of free gas, where the compressional velocity reaches its minimum with the increase of free gas saturation, hydrate increases compressional velocity by ~20 m/s for each 10% hydrate increment until all pores are filled with hydrate.

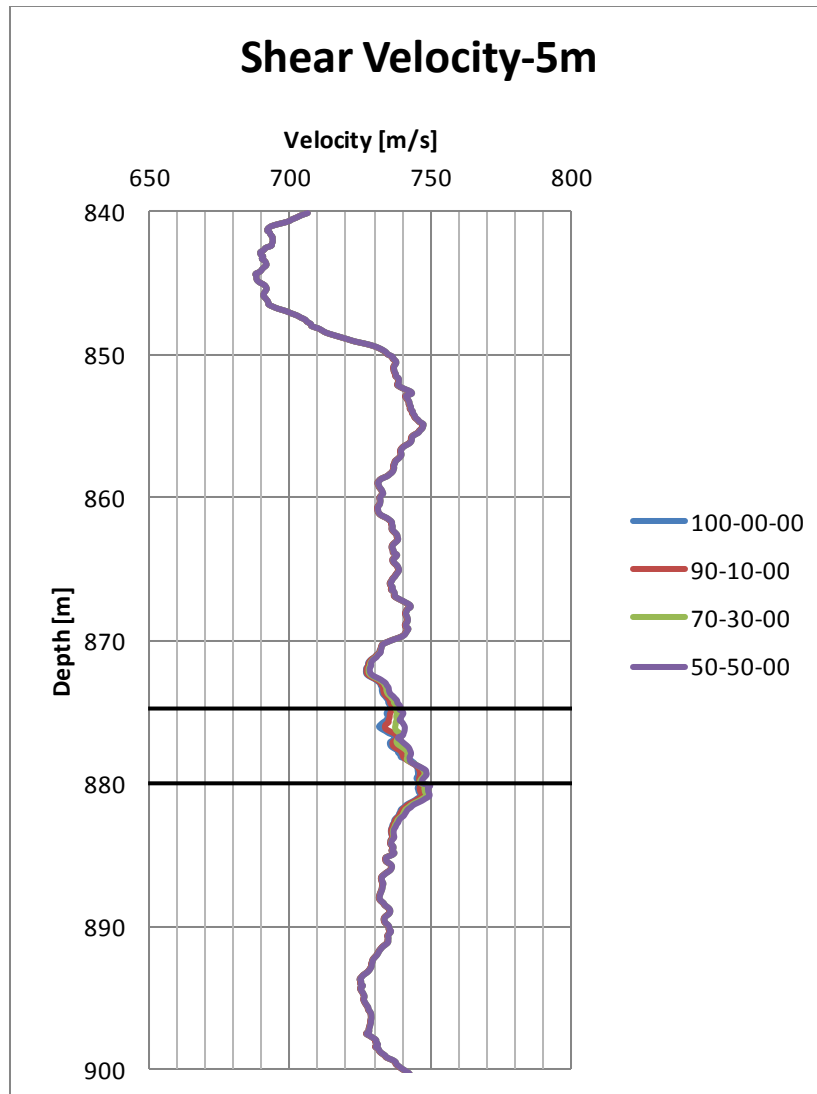


Figure 4.27: This figure presents the shear velocity versus depth for the Figure 4.26. The 5 m thick layer is filled with 10, 30, and 50% hydrate saturation. Results show that the hydrate saturation does not contribute or affect the shear velocity even in high hydrate saturation.

**Water-Hydrate-Free Gas Saturation (90-10-00-5m):**

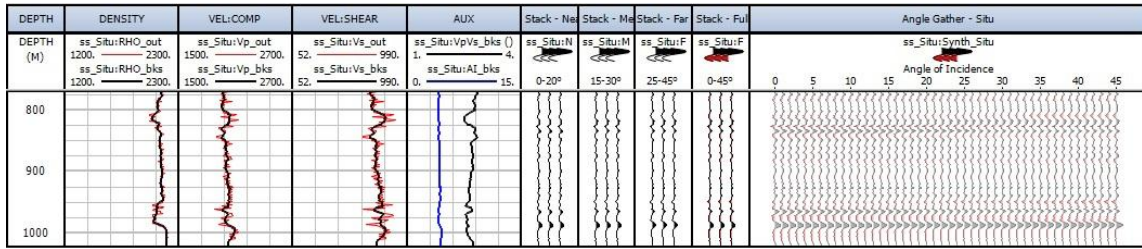


Figure 4.28: Seismic signature for a 2-phase zone containing 10% hydrate. Even though there is a slight increase of compressional velocity, the BSR is not visible. The result looks similar to Figure 4.12 where layers are 100% saturated with water. This shows that even 10% hydrate saturation does not contribute in the creation of the BSR.

**Water-Hydrate-Free Gas Saturation (70-30-00-5m):**

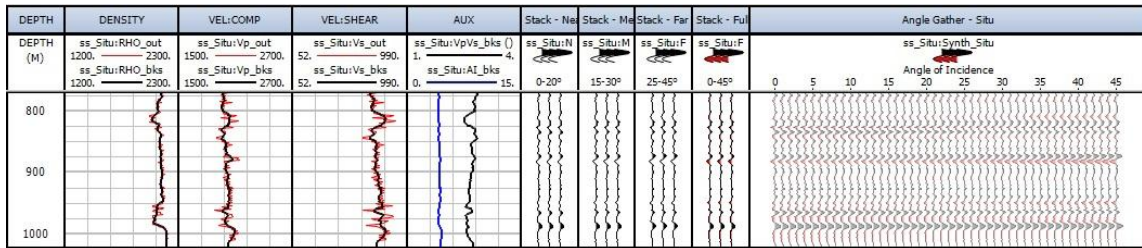


Figure 4.29: Seismic signature for a 2-phase zone containing 30% hydrate. With this hydrate saturation, the BSR is now visible. As expected, since hydrate increases the compressional velocity, the BSR signature starts with a peak unlike free gas scenarios were trough. Observing peak simply implies that the layer encountered is denser than the layer above and compressional velocity is higher.

**Water-Hydrate-Free Gas Saturation (50-50-00-5m):**

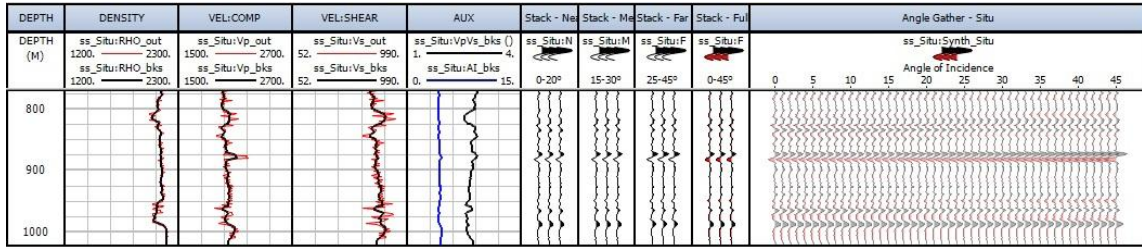


Figure 4.30. Seismic signature for a 2-phase zone containing 50% hydrate. The BSR is now visible and the peak is now easier to observe. Models in this section imply that hydrates are not the fluids to rely on when looking for the BSR, knowing that hydrates will not exceed 10% of the pores.

**4.4.2: High Hydrate with Low Free Gas**

Models in this section are created in order to observe how much free gas is needed to overcome the effect of 50% hydrate saturations in models shown in the previous section. As shown in Figure 4.31, small saturation of 1, 3, and 5% free gas is added while having constant 50% hydrate saturation.

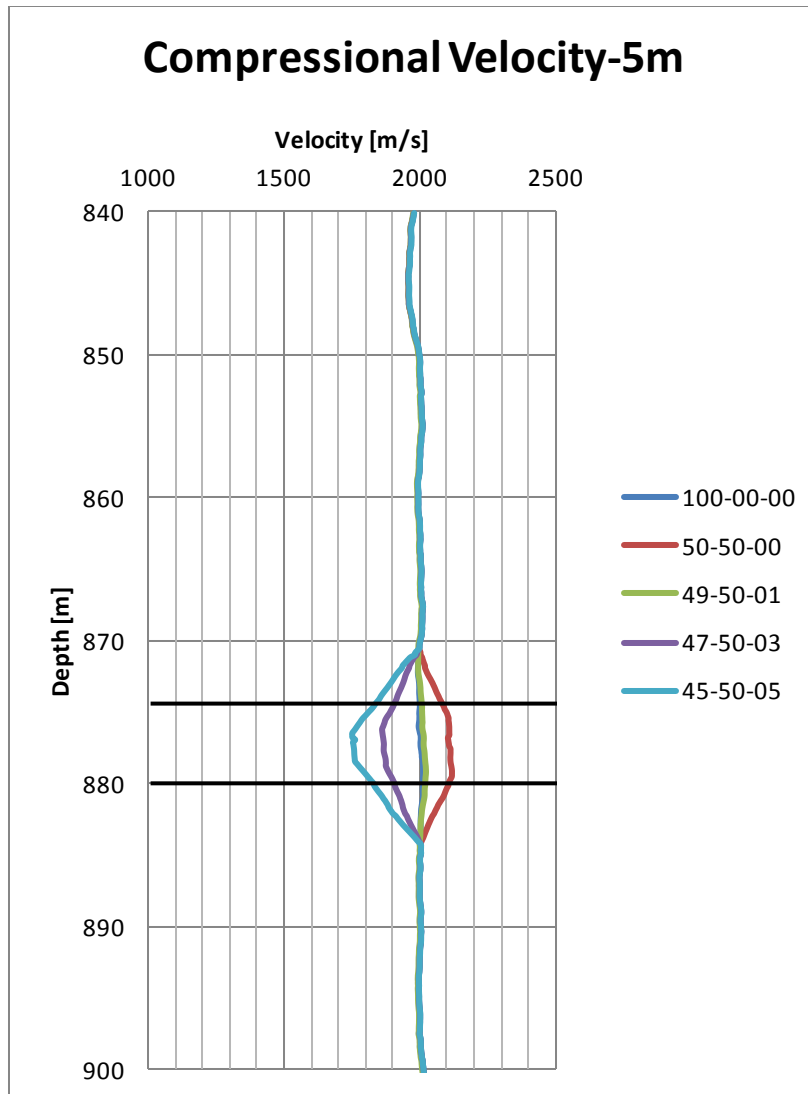


Figure 4.31: This figure presents the compressional velocity versus depth for the cases with 50% hydrate saturation and increasing free gas of 1, 3, and 5% saturation. It appears that with 1% free gas saturation, the compressional velocity decreases by ~100 m/s making its curve to almost match on top of 100% water saturation curve. For each extra 2% of free gas saturation, the compressional velocity continues to drop by ~120 m/s.

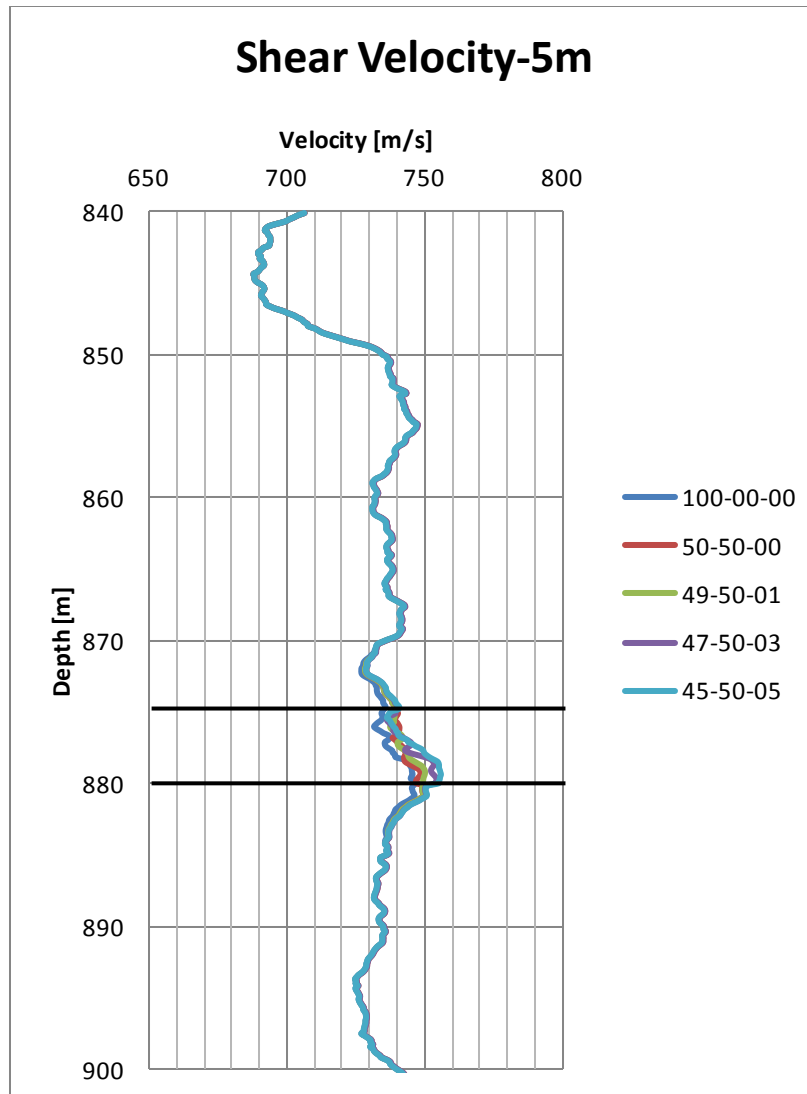


Figure 4.32: This figure presents the shear velocity versus depth for the cases with 50% hydrate saturation and increasing free gas of 1, 3, and 5% saturation. As the water is substituted with hydrate and/or these low percentages of free gas, the shear velocity increases. However, these changes are minimal and hard to observe.

**Water-Hydrate-Free Gas Saturation (49-50-01-5m):**

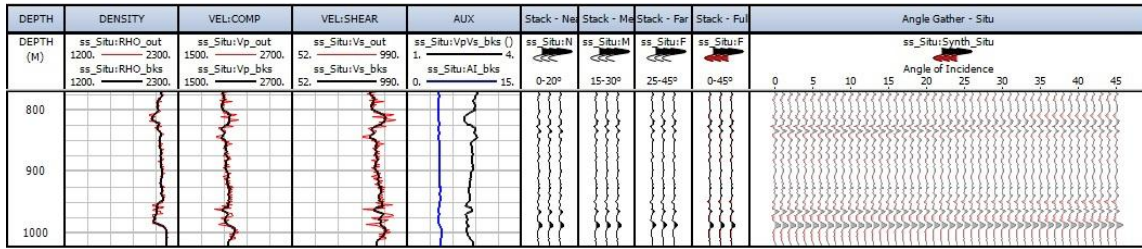


Figure 4.33: Seismic signature for a 3-phase zone containing 50% hydrate and 1% free gas (2-Phase zone containing 50% is presented in previous section, Figure 4.30). The BSR is now overshadowed due to presence of 1% free gas. This result matches with the compressional velocity result. Furthermore, this shows the importance of the free gas and how it can affect the BSR.

**Water-Hydrate-Free Gas Saturation (47-50-03-5m):**

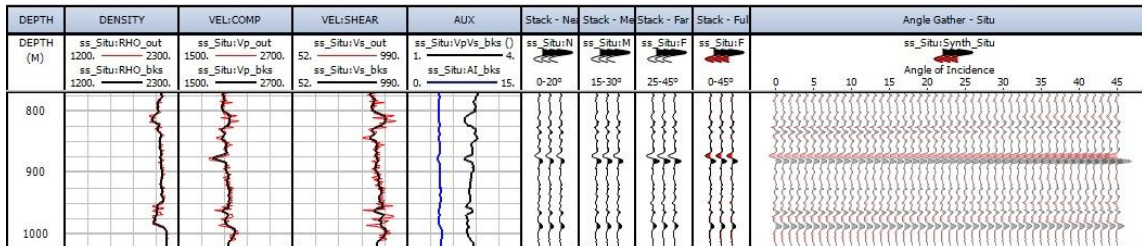


Figure 4.34: Seismic signature for a 3-phase zone containing 50% hydrate and 3% free gas. The addition of 2% free gas compared to the previous model will result in more reduction of the compressional velocity, thus making the BSR visible.

**Water-Hydrate-Free Gas Saturation (45-50-05-5m):**

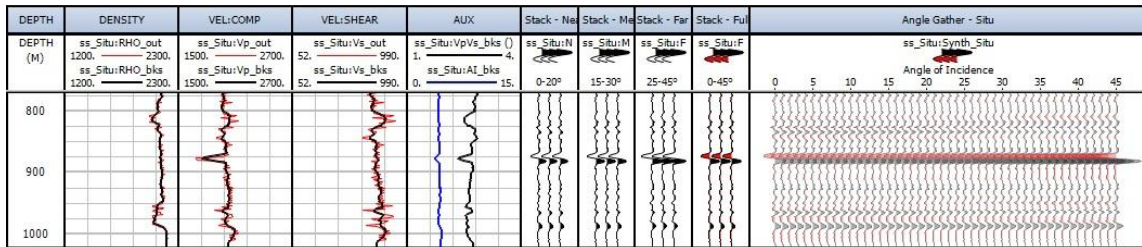


Figure 4.35: Seismic signature for a 3-phase zone containing 50% hydrate and 5% free gas. As the free gas is substituted for water by 5% compared to the previous case, a profound seismic signature of BSR is created. This is due to a significant reduction in compressional velocity.

#### 4.5: AMPLITUDE VERSUS ANGLE OF INCIDENCE

The results for this section are presented for future studies and researchers whom want to focus on geophysical studies of methane hydrates. In this section, the results for the amplitude versus angle of incidence are shown in tabular format.

##### *Fluid Saturation Comparison*

Water Saturation	Hydrate Saturation	Gas Saturation	Thickness	Amplitude @ 0	Amplitude @ 45
94	1	5	5	-0.03625	-0.072
89	1	10	5	-0.055	-0.11
84	1	15	5	-0.067	-0.13
69	1	30	5	-0.083	-0.165
49	1	50	5	-0.088	-0.178
97	3	0	5	0.0022	0.0024
92	3	5	5	-0.0365	-0.072
82	3	15	5	-0.065	-0.1275
67	3	30	5	-0.078	-0.016
47	3	50	5	-0.085	-0.178
95	5	0	5	0.0025	0.003
90	5	5	5	-0.0365	-0.0725
80	5	15	5	-0.065	-0.1275
65	5	30	5	-0.08	-0.016
45	5	50	5	-0.0875	-0.18

Table 4.1: Shows the values of amplitudes at an incidence angle of 0 and 45 degree for a 3-phase zone layer of 5 meters. A slight increase of amplitude occurs when hydrate saturation increases, while with an increase of gas the amplitude decreases.

**Thickness**

Water Saturation	Hydrate Saturation	Gas Saturation	Thickness	Amplitude @ 0	Amplitude @ 45
97	3	0	5	0.0022	0.0024
92	3	5	5	-0.0365	-0.072
82	3	15	5	-0.065	-0.1275
67	3	30	5	-0.078	-0.016
47	3	50	5	-0.085	-0.178
97	3	0	10	-0.0045	-0.00275
92	3	5	10	-0.041	-0.0725
82	3	15	10	-0.069	-0.1275
67	3	30	10	-0.0825	-0.1575
47	3	50	10	-0.088	-0.1725
97	3	0	30	0.00775	0.0035
92	3	5	30	-0.024	-0.0575
82	3	15	30	-0.0475	-0.1125
67	3	30	30	-0.5875	-0.1375
47	3	50	30	-0.6375	-0.1575

Table 4.2: Shows the values found for amplitudes at incidence angle of 0 and 45 degree, for a 3-phase zone layers containing constant hydrate saturation of 3%. Since the layers are heterogeneous at the reading points, only data from same thickness zone can be compared to one another.

**Pure Hydrate**

Water Saturation	Hydrate Saturation	Gas Saturation	Thickness	Amplitude @ 0	Amplitude @ 45
90	10	0	5	0.0035	0.0049
70	30	0	5	0.0088	0.0151
50	50	0	5	0.01475	0.027

Table 4.3: Shows the values found for amplitudes at incidence angle of 0 and 45 degree, for layers containing high hydrate saturation.

**High Hydrate with Low Free Gas**

Water Saturation	Hydrate Saturation	Gas Saturation	Thickness	Amplitude @ 0	Amplitude @ 45
50	50	0	5	0.015	0.027
49	50	1	5	0.0049	0.005
47	50	3	5	-0.016	-0.034
45	50	5	5	-0.03	-0.06

Table 4.4: Shows the values found for amplitudes at incidence angle of 0 and 45 degree, for layers containing high hydrate saturation and low gas saturation.

Results show that all of the models in which the gas saturation is more than 5%, class III AVO is encountered. This classifies the BSR as class III AVO.

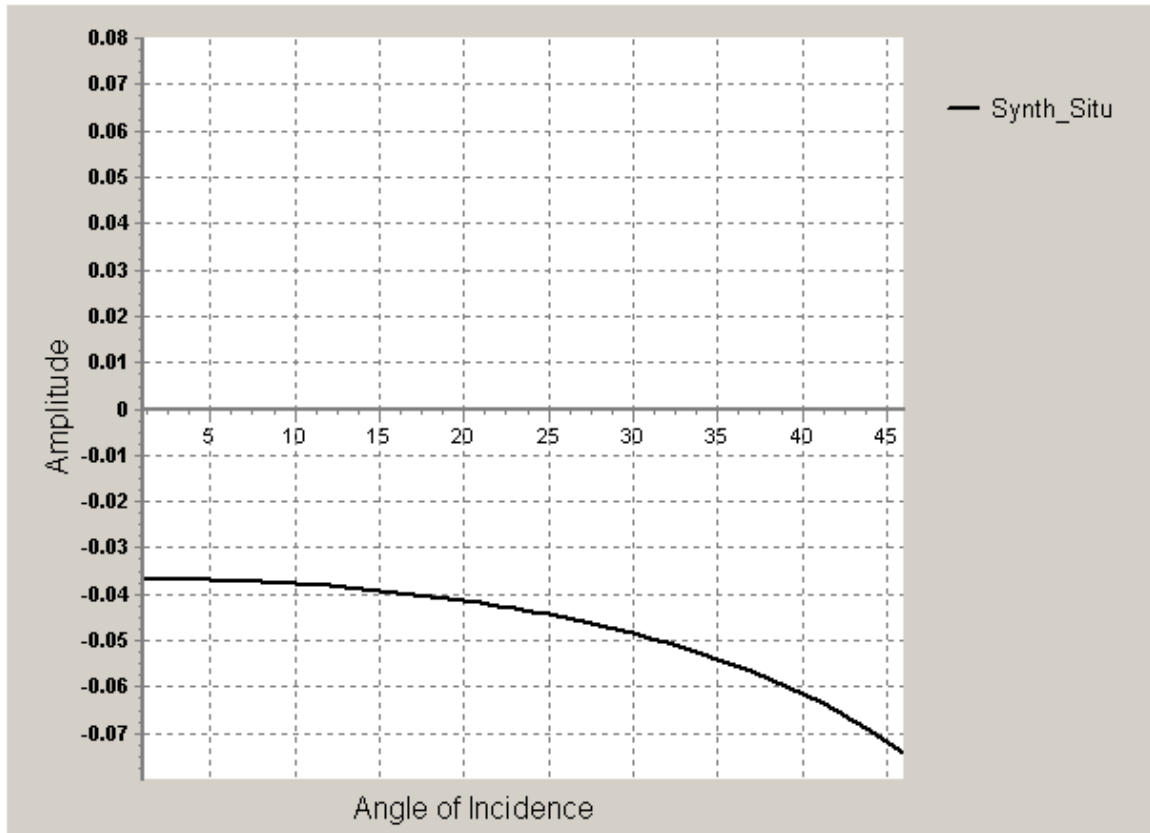


Figure 4.36: Amplitude versus angle of incidence for model 92-03-05 with 3-phase zone thickness of 5 m.

## **Chapter 5: Conclusion and Recommendations for Future Work**

### **5.1: SUMMARY AND CONCLUSIONS**

The main objectives of this thesis were: 1. To create synthetic seismograms for a discrete three-phase methane equilibrium zone. 2. To examine how fluid saturation variation and changing the thickness of the three-phase zone may affect the intensity of seismic signatures. Seismic prospecting was the main motivation of this research followed by the importance of hydrate as a potential source of energy, its influence on the global climate, and drilling hazard identification.

Using the well-logging data, the elastic properties of the formation were calculated via rock physics models. These data then were used to determine the acoustic velocities. Interactive Petrophysics software convoluted these acoustic velocities with the actual wavelet to create synthetic seismograms.

Results show that the main factor for the intensity of the BSR is the abundance of the free gas in the three-phase zone. Regardless of the amount of the hydrate, 5% of gas saturation in the formation makes the BSR to be visible. In the other hand, methane hydrate has a minimal contribution in intensity of the BSR. Minimum of 50% methane hydrate saturation is required in the formation before BSR becomes observable in the synthetic seismogram. Furthermore, from special cases it was found that 50% hydrate saturation and 1 % gas saturation cancel each other out and result in no BSR. This means that increase of compressional velocity by 50% hydrate saturation is equivalent to the decrease of compressional velocity of 1% gas saturation.

## 5.2: RECOMMENDATIONS FOR FUTURE WORK

The recommendations for future studies in the same area are presented as follows:

- It is recommended to create models for sandstones. Studies show that the thickness of the three-phase zone in sandstones is about two orders of magnitude smaller than in clays. Since the thickness of the 3-phase zone in sandstones is in order of a few cm, the change in BSR may or may not be visible as a result of the presence of a 3-phase zone.
- This study uses the no contact-cement rock physics model. Other contact models can be used to create synthetic seismograms. This will result in different fluid saturation models which can greatly change the results.
- Randomizing the fluid saturation throughout the three-phase zone, rather than having one homogenous formation can make the model more realistic.
- Following the AVO classification, further AVO interpretation such as cross-plotting, noise filtration, Lambda-mu-rho (LMR), and neural network AVO analysis can be done.
- Lastly, seismic inversion is the next step. In this process, seismic reflectivity is transformed to acoustic impedance. This will allow us to use the seismic response to extract subsurface geological information.

## Acronyms

AVO	:	Amplitude Versus Offset
BSR	:	Bottom-Simulating Reflection
GHSZs	:	Gas Hydrate Stability Zones
mbsf	:	Meters Below Sea Floor
ODP	:	Ocean Drilling Program

## Nomenclature

### Parameters

$G$	:	Shear Moduli
$G_{\text{dry}}$	:	Dry Shear Moduli
$G_{\text{HM}}$	:	Hertz Mindlin Shear Moduli
$G_{\text{sat}}$	:	Saturated Shear Moduli
$K$	:	Bulk Moduli
$K_{\text{dry}}$	:	Dry Bulk Moduli
$K_{\text{dry-Wood}}$	:	Dry Bulk Modulus by Wood
$K_f$	:	Bulk Modulus of the Pore Fluid
$K_g$	:	Bulk Modulus of Gas
$K_h$	:	Bulk Modulus of Hydrate
$K_{\text{HM}}$	:	Hertz Mindlin Bulk Moduli
$K_{\text{sat}}$	:	Saturated Bulk Moduli
$K_w$	:	Bulk Modulus of Water
$n$	:	The Average number of Contact Per Grain
$P$	:	Effective Pressure
$R$	:	Reflection Coefficient
$S_g$	:	Gas Saturation
$S_h$	:	Hydrate Saturation
$S_w$	:	Water Saturation
$V_p$	:	Compressional Velocity
$V_s$	:	Shear Velocity
$Z$	:	Acoustic Impedance of the Formation

### **Greek Symbols**

$\rho$	:	Density of the Formation
$\rho_f$	:	Density of the Pore Fluid
$\rho_s$	:	Bulk Density of the Solid Phase
$\emptyset$	:	Porosity
$\emptyset_c$	:	Critical Porosity
$\nu$	:	Poisson's Ratio

## References

- Aki, K. and P. G. Richards. "Quantitative Seismology: Theory and Methods." W. H. Freeman and Co. 1980.
- Archer, D., Buffett, B., and Brovkin, V. "Ocean Methane Hydrates as a Slow Tipping Point in the Global Carbon Cycle." *Proceedings of the National Academy of Sciences*, vol. 106, no. 49, 2008, pp. 20596–20601. doi:10.1073/pnas.0800885105.
- Bahadori, Alireza. *Natural Gas Processing: Technology and Engineering Design*. Amsterdam, Elsevier, 2014.
- Berndt, C., Bünz, S., Clayton, T., Mienert, J., and Saunders, M. "Seismic Character of Bottom Simulating Reflectors: Examples from the Mid-Norwegian Margin." *Marine and Petroleum Geology*, vol. 21, no. 6, 2004, pp. 723–733. doi:10.1016/j.marpetgeo.2004.02.003.
- Berryman, James G. "Origin of Gassmann's Equations." *Geophysics*, vol. 64, no. 5, 1999, pp. 1627–1629. doi:10.1190/1.1444667.
- Bihani, Abhishek D. "Pore Size Distribution and Methane Equilibrium Conditions at Walker Ridge Block 313 Northern Gulf of Mexico" M.S. Thesis, University of Texas at Austin, Austin, Texas, 2016.
- Bryan, George M. "In Situ Indications of Gas Hydrate." *Natural Gases in Marine Sediments*, 1974, pp. 299–308. doi:10.1007/978-1-4684-2757-8\_17.
- Carcione, José M., and Umberta Tinivella. "Bottom Simulating Reflectors: Seismic Velocities and AVO Effects." *Geophysics*, vol. 65, no. 1, 2000, pp. 54–67. doi:10.1190/1.1444725.
- Castagna, J. P., Swan, H. W., and Foster, D. J. "Framework for AVO Gradient and Intercept Interpretation." *Geophysics*, vol. 63, no. 3, 1998, pp. 948–956. doi:10.1190/1.1444406.
- Collett, Timothy S. "Energy Resource Potential of Natural Gas Hydrates." *AAPG Bulletin*, vol. 86, 2002, doi:10.1306/61e2dd2-173e-11d7-8645000102c1865d.
- Collett, T. S., Lee, M. W., Zyrianova, M. V., Mrozewski, S. A., Guerin, G., Cook, A. E., and Goldberg, D. S. "Gulf of Mexico Gas Hydrate Joint Industry Project Leg II Logging-While-Drilling Data Acquisition and Analysis." *Marine and Petroleum Geology*, vol. 34, no. 1, 2012, pp. 41–61. doi:10.1016/j.marpetgeo.2011.08.003.

- Dickens, G. R., O'neil, J. R., Rea, D. K., and Owen, R. M. "Dissociation of Oceanic Methane Hydrate as a Cause of the Carbon Isotope Excursion at the End of the Paleocene." *Paleoceanography*, vol. 10, no. 6, 1995, pp. 965–971. doi:10.1029/95pa02087.
- Dvorkin, Jack, and Amos Nur. "Elasticity of High Porosity Sandstones: Theory for Two North Sea Data Sets." *Geophysics*, vol. 61, no. 5, 1996, pp. 1363–1370. doi:10.1190/1.1444059.
- Dvorkin, J., Prasad, M., Sakai, A., and Lavoie, D. "Elasticity of Marine Sediments: Rock Physics Modeling." *Geophysical Research Letters*, vol. 26, no. 12, 1999, pp. 1781–1784. doi:10.1029/1999gl900332.
- Ecker, Christine, and David E. Lumley. "Seismic AVO Analysis of Methane Hydrate Structures." *SEG Technical Program Expanded Abstracts 1994*, 1994, doi:10.1190/1.1822708.
- Ecker, C., Dvorkin, J., and Nur, A. M. "Estimating the Amount of Gas Hydrate and Free Gas from Marine Seismic Data." *Geophysics*, vol. 65, no.2, 2000, pp. 565–573. doi:10.1190/1.1444752.
- Ecker, C., Dvorkin, J., and Nur, A. "Sediments with Gas Hydrates: Internal Structure from Seismic AVO." *SEG Technical Program Expanded Abstracts 1996*, 1996, doi:10.1190/1.1826475.
- Energy from Gas Hydrates: Assessing the Opportunities & Challenges for Canada.* Ottawa, Council of Canadian Academies, 2008.
- Frye, M., Shedd, W., and Boswell, R. "Gas Hydrate Resource Potential in the Terrebonne Basin, Northern Gulf of Mexico." *Marine and Petroleum Geology*, vol. 34, no. 1, 2012, pp. 150–168. doi:10.1016/j.marpetgeo.2011.08.001.
- Gassmann, Fritz. "Elastic Waves Through A Packing Of Spheres." *Geophysics*, vol. 16, no. 4, 1951, pp. 673–685. doi:10.1190/1.1437718.
- Guerin, G., Goldberg, D., and Meltser, A. "Characterization of in Situ Elastic Properties of Gas Hydrate-Bearing Sediments on the Blake Ridge." *Journal of Geophysical Research: Solid Earth*, vol. 104, no. B8, Oct. 1999, pp. 17781–17795. doi:10.1029/1999jb900127.
- Haacke, R. R., Westbrook, G. K., and Hyndman, R. D. "Gas Hydrate, Fluid Flow and Free Gas: Formation of the Bottom-Simulating Reflector." *Earth and Planetary Science Letters*, vol. 261, no. 3-4, 2007, pp. 407–420. doi:10.1016/j.epsl.2007.07.008.

- Hamilton, Edwin L. "Elastic Properties of Marine Sediments." *J. Geophys. Res. Journal of Geophysical Research*, vol. 76, no. 2, Oct. 1971, pp. 579–604. doi:10.1029/jb076i002p00579.
- Holbrook, W. S. et al. "Methane Hydrate and Free Gas on the Blake Ridge from Vertical Seismic Profiling." *Science*, vol. 273, no. 5283, 1996, pp. 1840–1843. doi:10.1126/science.273.5283.1840.
- Kvenvolden, Keith A. "Gas Hydrates--Geological Perspective and Global Change." *Reviews of Geophysics*, vol. 31, no. 2, 1993, p. 173. doi:10.1029/93rg00268.
- Lee, G. H., Kim, H. J., Jou, H. T., and Cho, H. M. "Opal-A/Opal-CT Phase Boundary Inferred from Bottom-Simulating Reflectors in the Southern South Korea Plateau, East Sea (Sea of Japan)." *Geophysical Research Letters*, vol. 30, no. 24, 2003, doi:10.1029/2003gl018670.
- Max, M. D., Johnson, A. H., and Dillon, W. P. "Introduction: Economic Geology of Natural Gas Hydrate." *Coastal Systems and Continental Margins Economic Geology of Natural Gas Hydrate*, pp. 1–16. doi:10.1007/1-4020-3972-7\_1.
- Mienert, J., Vanneste, M., Bünz, S., Andreassen, K., Haflidason, H., and Sejrup, H. P. "Ocean Warming and Gas Hydrate Stability on the Mid-Norwegian Margin at the Storegga Slide." *Ormen Lange—An Integrated Study for Safe Field Development in the Storegga Submarine Area*, 2005, pp. 233–244. doi:10.1016/b978-0-08-044694-3.50024-x.
- Milkov, Alexei V. "Global Estimates of Hydrate-Bound Gas in Marine Sediments: How Much Is Really out There?" *Earth-Science Reviews*, vol. 66, no. 3-4, 2004, pp. 183–197.
- Mindlin, R. D. "Compliance of Elastic Bodies in Contact." *The Collected Papers of Raymond D. Mindlin Volume I*, 1949, pp. 259–268. doi:10.1007/978-1-4613-8865-4\_24.
- Murata, K. J., and J. K. Nakata. "Cristobalitic Stage in the Diagenesis of Diatomaceous Shale." *Science*, vol. 184, no. 4136, Mar. 1974, pp. 567–568. doi:10.1126/science.184.4136.567.
- Murphy, W. F. I., "Effects of Microstructure and Pore Fluids on the Acoustic Properties of Granular Sedimentary Materials" Ph.D. thesis, Stanford University, Stanford, California, 1982.

- “NOAA Ocean Explorer: Windows to the Deep: Phase Diagram for Gas Hydrate.” *NOAA Ocean Explorer Podcast RSS 20*, NOAA Ocean Explorer Webmaster, 26 Aug. 2010, [oceanexplorer.noaa.gov/explorations/03windows/background/hydrates/media/fig1\\_phase\\_diagram.html](http://oceanexplorer.noaa.gov/explorations/03windows/background/hydrates/media/fig1_phase_diagram.html).
- Nur, A. M., Mavko, G., Dvorkin, J., and Gal, D. “Critical Porosity: The Key to Relating Physical Properties to Porosity in Rocks.” *SEG Technical Program Expanded Abstracts 1995*, 1995, doi:10.1190/1.1887540.
- Paull, C.k., and R. Matsumoto. “Leg 164 Overview.” *Proceedings of the Ocean Drilling Program Proceedings of the Ocean Drilling Program, 164 Scientific Results*, 2000, doi:10.2973/odp.proc.sr.164.204.2000.
- Paull, C. K., Matsumoto, R., Wallace, P. J., et al. “Proceedings of the Ocean Drilling Program, 164 Initial Reports.” *Proceedings of the Ocean Drilling Program*, 1996, doi:10.2973/odp.proc.ir.164.108.1996.
- Rutherford, Steven R., and Robert H. Williams. “Amplitude-versus-Offset Variations in Gas Sands.” *Geophysics*, vol. 54, no. 6, 1989, pp. 680–688. doi:10.1190/1.1442696.
- Senergy Software Ltd, “Interactive Petrophysics User Manual.” *Interactive Petrophysics Users Manual 2014*, Scotland: Senergy Software LTd.
- Sloan, E. Dendy. “Gas Hydrates: Review of Physical/Chemical Properties.” *Energy & Fuels*, vol. 12, no. 2, 1998, pp. 191–196. doi:10.1021/ef970164 .
- Stewart, R. R., Huddleston, P. D., and Kan, T. K. “Seismic versus Sonic Velocities: A Vertical Seismic Profiling Study.” *Geophysics*, vol. 49, no. 8, 1984, pp. 1153–1168. doi:10.1190/1.1441745.
- Tréhu , A., Ruppel, C., Holland, M., Dickens, G., Torres, M., Collett, T., Goldberg, D., Riedel, M., and Schultheiss, P. “Gas Hydrates in Marine Sediments: Lessons from Scientific Ocean Drilling.” *Oceanog. Oceanography*, vol. 19, no. 4, Jan. 2006, pp. 124–142. doi:10.5670/oceanog.2006.11.
- Waite, W. F., Stern, L. A., Kirby, S. H., Winters, W. J., and Mason, D. H. “Simultaneous Determination of Thermal Conductivity, Thermal Diffusivity and Specific Heat in SI Methane Hydrate.” *Geophysical Journal International*, vol. 169, no. 2, 2007, pp. 767–774. doi:10.1111/j.1365-246x.2007.03382.x.
- Wood, A. B. *A Textbook of Sound*. London, G. Bell, 1941.

Zoeppritz, K. Erdbebenwellen VII, VII B, “Über Reflexion und Durchgang seismischer Wellen Durch Unstetigkeitsflächen [On the Reflection and Transmission of Seismic Wave at Surfaces of Discontinuity]” Nachrichten von der Koniglichen Gesellschaft der Wissenschaften zu Gottingen, Mathematisch-Physikalische Klasse, 66-84.